A MEASUREMENT OF THE $^{12}C(n,2n)^{11}C$ CROSS-SECTION FOR USE AS AN INERTIAL CONFINEMENT FUSION DIAGNOSTIC

By

Garrett E. Hartshaw

A thesis submitted in partial fulfillment of the
requirements for the degree of

Bachelor of Science

Houghton College

May 2014

……..……..……..

Department of Physics
May 6, 2014

……..

Dr. Mark Yuly
Professor of Physics
Research Supervisor

……..

Dr. Brandon Hoffman
Associate Professor of Physics

A MEASUREMENT OF THE $^{12}C(n,2n)^{11}C$ CROSS-SECTION FOR USE AS AN INERTIAL CONFINEMENT FUSION DIAGNOSTIC

By

Garrett E. Hartshaw

Submitted to the Department of Physics
on May 6, 2014 in partial fulfillment of the
requirement for the degree of
Bachelor of Science

Abstract

In inertial confinement fusion (ICF), nuclear fusion reactions are initiated by bombarding a small fuel pellet with high power lasers. One ICF diagnostic involves measuring the high-energy neutron yield via activation of ^{12}C, requiring an accurate value for the $^{12}C(n,2n)^{11}C$ cross-section. An experiment to determine this cross-section in the energy range of 20-27 MeV was performed using the tandem van de Graaff accelerator at Ohio University. Monoenergetic neutrons, produced via the $T(d,n)\alpha$ reaction, were allowed to strike targets of polyethylene and graphite. Target activation was determined by counting positron annihilations due to β^+ decay using back-to-back NaI detectors and the neutron flux was determined indirectly via protons elastically scattered from the polyethylene target. The cross-section will be determined from the number of ^{11}C present in the target after activation, the number of protons detected during activation, and the geometry of the experiment. Funded in part by a LLE contract through the DOE.

Thesis Supervisor: Dr. Mark Yuly
Title: Professor of Physics

TABLE OF CONTENTS

TABLE OF FIGURES

Chapter 1

FUSION

Nuclear fusion, now known to be the process that powers the sun, is the process by which nuclei can be combined, at high temperatures and pressures. For reactant nuclei lighter than iron, the mass of the product nucleus is lighter than the combined mass of the reactant nuclei, with the difference in mass released as energy. In the century after the discovery of this process, there has been a sustained effort to control this process with conditions achievable on Earth.

1.1 History

The discovery of nuclear fusion was based upon two earlier developments. The first, in 1905, was the theory of special relativity and its resultant equivalence of mass and energy [1]. The second, in 1919, was the invention of the mass spectrometer [2] leading to the discovery that the mass of helium was slightly less than the expected four times the mass of hydrogen. Additionally, the age of the Earth was discovered to be much older than previously thought [3], requiring a theory on the mechanism of the sun's energy that would allow it to survive as long as was now necessary. In 1922, as a result of these factors, it was suggested that the transmutation of hydrogen into helium was in fact the source of the sun's energy [3].

As a prerequisite for nuclear fusion, it is necessary for the two nuclei involved to approach to within about 1.7 fm, at which point the residual nuclear strong force overcomes the Coulomb repulsion between the nuclei. When it was first proposed, fusion was thought unlikely due to the height of the potential energy peak. With the discovery of quantum tunneling, it became apparent that fusion could occur at lower temperatures, as the incoming nucleon could tunnel through the electrostatic potential barrier, as shown in Figure 2.

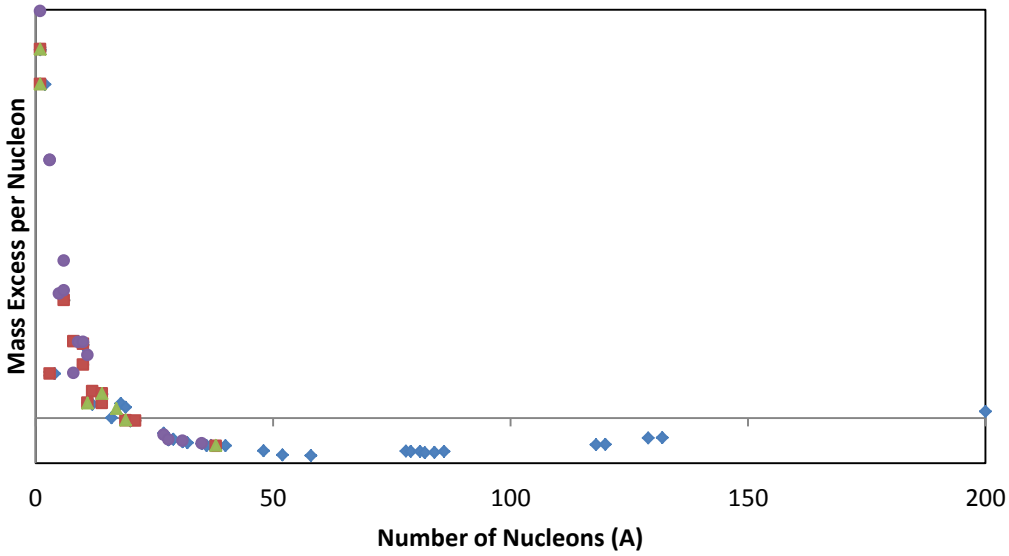

Figure 1: Mass excess per nucleon vs. number of nucleons measured in the late 1930s. Values from Aston's [4], Bainbridge and Jordan's [5], and Mattauch's [6] mass spectrographs are shown in blue diamonds, red squares, and green triangles respectively. The purple circles are based on reactions performed by Livingston and Bethe [7]. The energy released in a nuclear process, be it fusion or fission, is equal to the difference in mass between the products and the reactants. For all nucleons lighter than iron energy is released during fusion, while for those heavier than iron energy is required for fusion.

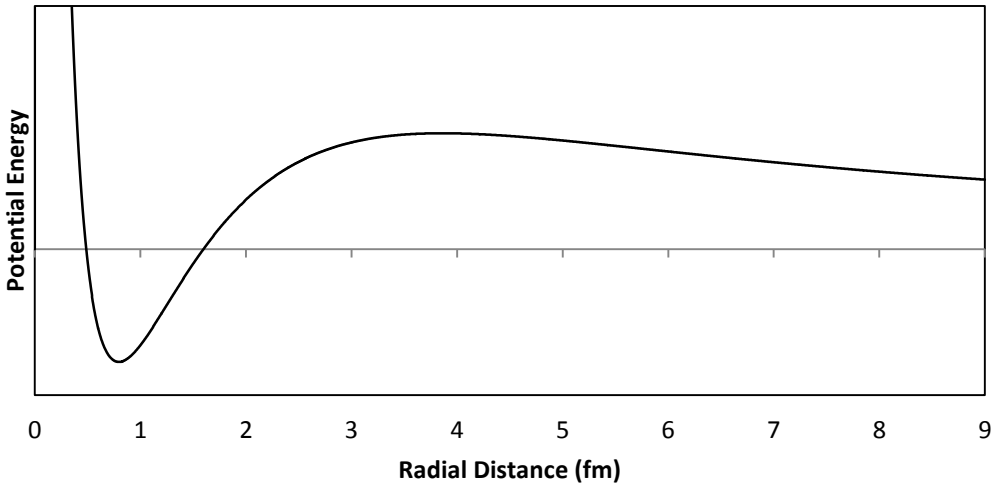

Figure 2: Conceptual plot of the potential energy between two nuclei as a function of radius. At large distances, greater than around 3 fm, electrostatic repulsion is the dominant force. As the nuclei approach within the range of the nuclear strong force, at a distance of around 3 fm, this potential begins to drop off, having a minimum at around 0.7 fm.

For a nuclear fusion reaction to output enough energy to be self-sustaining, a condition known as ignition, it must be both heated and confined, as shown by Lawson in 1957 [8]. In the ideal case that a plasma with number density n is heated to a temperature T, and this temperature is maintained for a time t, the ratio of the energy released to the energy supplied is given by

$$R = \frac{\frac{P_R}{3n^2 k_B T}}{\frac{P_B}{3n^2 k_B T} + \frac{1}{nt}} \tag{1}$$

where P_R and P_B are, respectively, the power produced by the reaction and power radiated from the plasma per unit volume and $k_B = 8.61\times10^{-5}$ eV/K is the Boltzmann constant. For a system to have net power gain, it must be the case that

$$\eta(R + 1) > 1 \tag{2}$$

where η is the efficiency of feeding the released energy back into the reaction.

This condition may be achieved in a controlled manner in three known ways. The first, gravitational confinement is the method occurring in the sun, but due to the weakness of the gravitational force is unable to be achieved on earth. In the second method, magnetic confinement fusion, the nuclei are confined by magnetic fields, and then heated; either as a side effect of the magnetic confinement or by other means. In the third method, inertial confinement fusion, a very small amount of the fuel is compressed so suddenly that the inertia of the particles allows this compression to be maintained until the fusion reaction initiates.

1.1.1 Magnetic Confinement

The confinement of plasmas using magnetic fields is a result of a phenomenon known as Z-pinch. If two wires have current running in the same direction, they experience an attractive force due to the magnetic fields they generate. This same effect is also seen in an electrically conductive plasma: when a high current is run across a plasma, the resulting magnetic field has a focusing effect [9]. This pinch

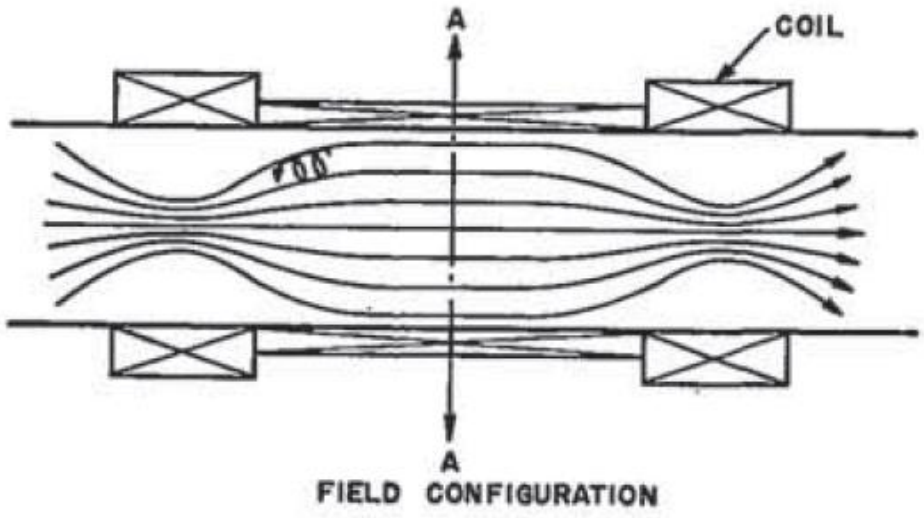

Figure 3: Schematic of magnetic field lines in a mirror machine. The larger coils at either end of the machine lead to an increasing magnetic field, thereby trapping charged particles within. Figure taken from Reference 10.

only confines radially, however, so in a linear z-pinch machine all of the plasma is quickly lost out of the ends.

There are two ways of solving this problem, both having difficulties. The first is to use what is known as the magnetic mirror effect to create a **mirror machine,** shown in Figure 3. A region in which the magnetic field strength increases in the direction parallel to the magnetic field lines tends to repel charged particles, so increasing the field strength at the ends of a linear z-pinch can increase the particle confinement time [10]. This mirror effect occurs as a result of the corkscrew movement of a charged particle in a magnetic field. For such a particle, the magnetic moment, given by

$$\mu = \frac{mv_{\perp}^2}{2B}, \tag{3}$$

remains constant, so in an increasing magnetic field B, the velocity perpendicular to the magnetic field, $v_{\perp}$, must also increase. The total energy of the particle, given by

$$\epsilon = qE + \mu B + \frac{1}{2}mv_{\parallel}^2 + \frac{1}{2}mv_{\perp}^2, \tag{4}$$

also is constant. For this to occur when the perpendicular velocity increases, the velocity parallel to the magnetic field, $v_{\parallel}$, must decrease, thereby confining the particle. This confinement is not perfect, however, and there are still losses through the ends of the machine.

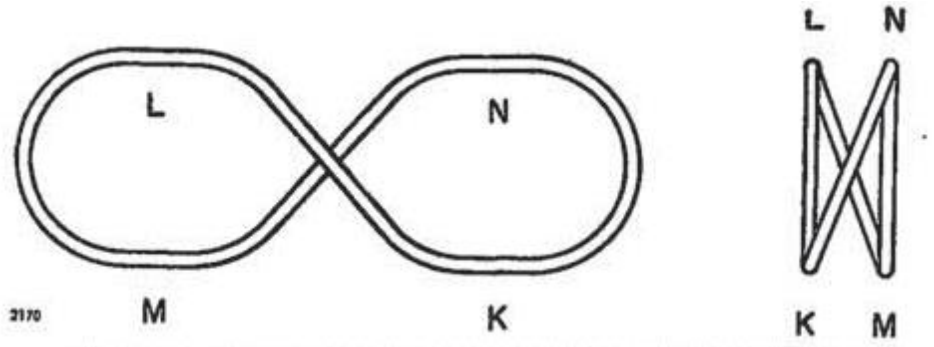

Figure 4: Top and end views of a figure-eight stellerator. As the two ends of the tube are curved in opposite directions, particles on the outside between L and M are on the inside between N and M and vice-versa. As a result, the drifts produced in these two regions cancel each other. Figure taken from Reference 12.

The second method to combat the problem of end losses is to connect the two ends of the z-pinch into a torus. However, this curvature causes the generated magnetic field to no longer be axially symmetric, resulting in drifts which result in the plasma being pushed toward the wall [11]. This effect can be overcome by twisting the torus into a figure eight [12], creating a device known as a **stellerator,** shown in Figure 4. A similar effect can also be produced in a simple torus by adding additional external coils, which twist the magnetic field.

Both of these magnetic z-pinch confinement methods become unstable for large magnetic fields at high temperatures [13]. This instability can be reduced by introducing an additional toroidal magnetic field in addition to the poloidal field created by the pinch [14], shown in Figure 5. This configuration was later refined into the **tokamak** by increasing the strength of the toroidal magnetic field [15]. In a

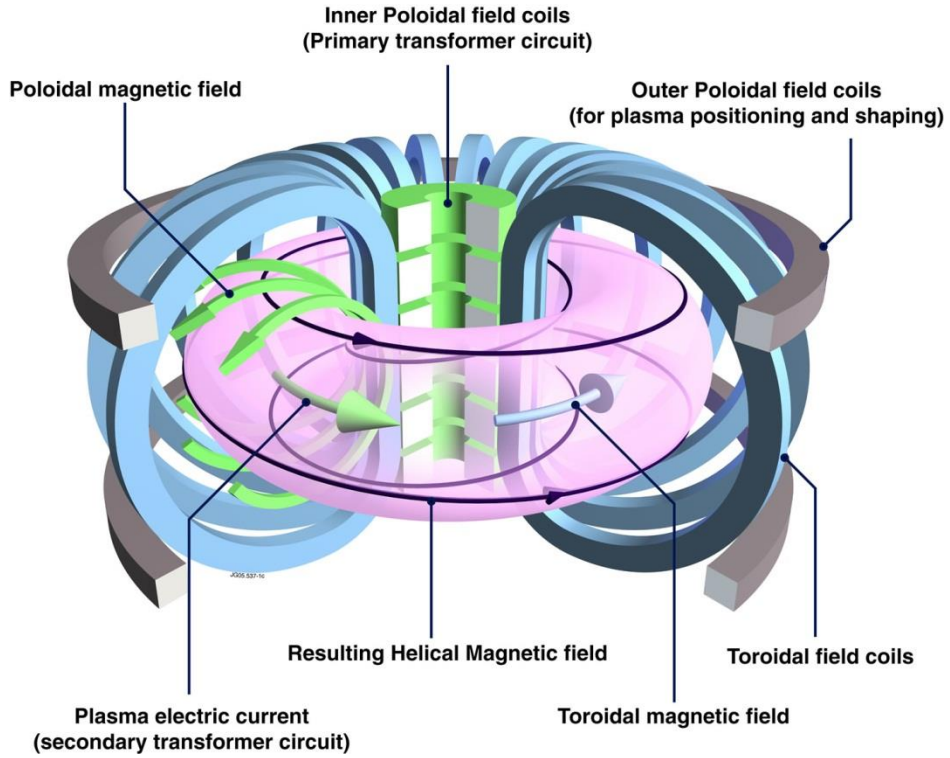

Figure 5: A schematic diagram of a tokamak. The poloidal field, generated by current flowing through the plasma, compresses the plasma while the toroidal field, generated by the external wire coils stabilizes it. Figure taken from Reference 16.

tokamak, the toroidal field is stronger than the poloidal, while in a stabilized stellerator this is reversed

Work on magnetic confinement fusion is continuing, with larger tokamaks being built in an effort to reach breakeven. The largest currently operating tokamak is the Joint European Torus (JET) built in 1983 [16], and construction of the larger ITER tokamak [17] is currently underway. The design of ITER is such that it is expected to be able to produce a net power output.

1.1.2 Inertial Confinement

Inertial confinement fusion (ICF) is the process of initiating fusion by compressing the fuel so rapidly that its inertia allows it to fuse before the electrostatic repulsion blows the fuel apart. The fusion (or hydrogen) bomb was the first artificial use of inertial confinement fusion, the deuterium fuel being heated by a fission reaction within the bomb itself, as shown in Figure 6 [18].

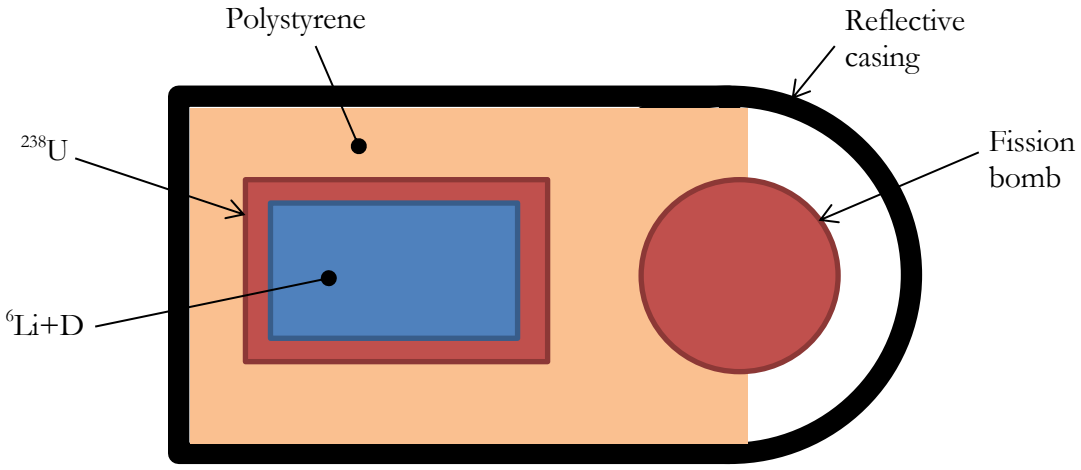

Figure 6: One possible version of a hydrogen bomb. A initial fission reaction is used to compress a lithium and deuterium fuel mixture. High-energy neutrons from the fission reaction create tritium via the reaction in Equation (8), which then undergoes fusion. The uranium shell surrounding the fusion fuel provides additional compression.

Most inertial confinement fusion research at present is performed using high-power lasers, this technique being first demonstrated in 1968 [19]. Due to the massive power necessary to compress the fuel pellets, very few facilities can perform ICF. In the United States, these are the OMEGA laser system at the University of Rochester's Laboratory for Laser Energetics (LLE), shown in Figure 7, and the National Ignition Facility (NIF) at the Lawrence Livermore National Lab (LLNL).

Originally, inertial confinement fusion was performed by focusing the laser beams directly onto the fuel pellet, a technique, shown in Figure 8, now known as direct drive ICF. This supplies the maximum amount of power to the fuel; however, a large number of laser beams are necessary to achieve the requisite spherical symmetry during compression. The number of beams necessary can be reduced using indirect drive ICF. In this process, the laser beams are instead focused on the inside of a small metal capsule known as a hohlraum, shown in Figure 9, which surrounds the fuel pellet. The hohlraum emits x-rays, which uniformly heat the outer shell of the fuel pellet. This causes the outer

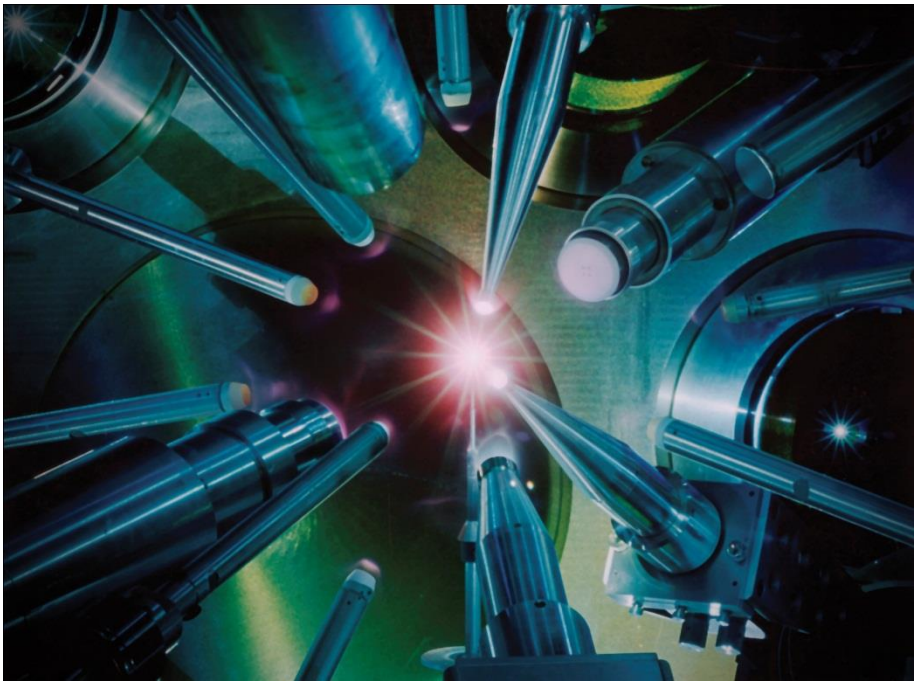

Figure 7: The inside of the target chamber of the OMEGA laser system at the University of Rochester's Laboratory for Laser Energetics. The beams can be seen to converge at the center of the image with various sensors positioned around the reaction center.

shell to vaporize, thereby compressing the remainder of the fuel pellet. Both the OMEGA laser and the NIF are able to perform either direct or indirect drive.

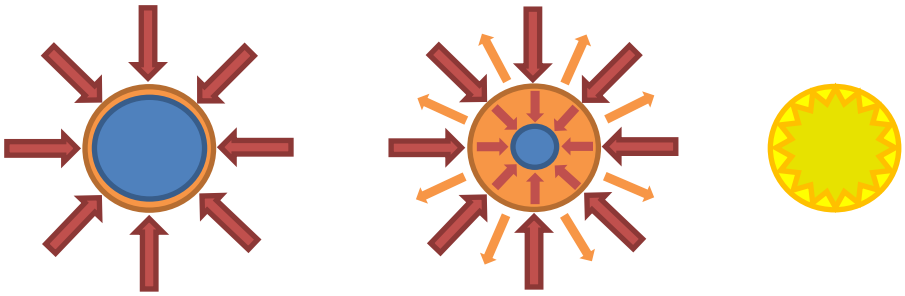

Figure 8: The inertial confinement fusion process. (a) The fuel pellet is uniformly heated by laser beams, for direct drive, or x-rays produced by a hohlraum, for indirect drive. (b) The outer layers of the fuel pellet are ablated, compressing the interior of the fuel pellet. (c) The fusion reaction can occur at maximum compression, releasing large amounts of energy.

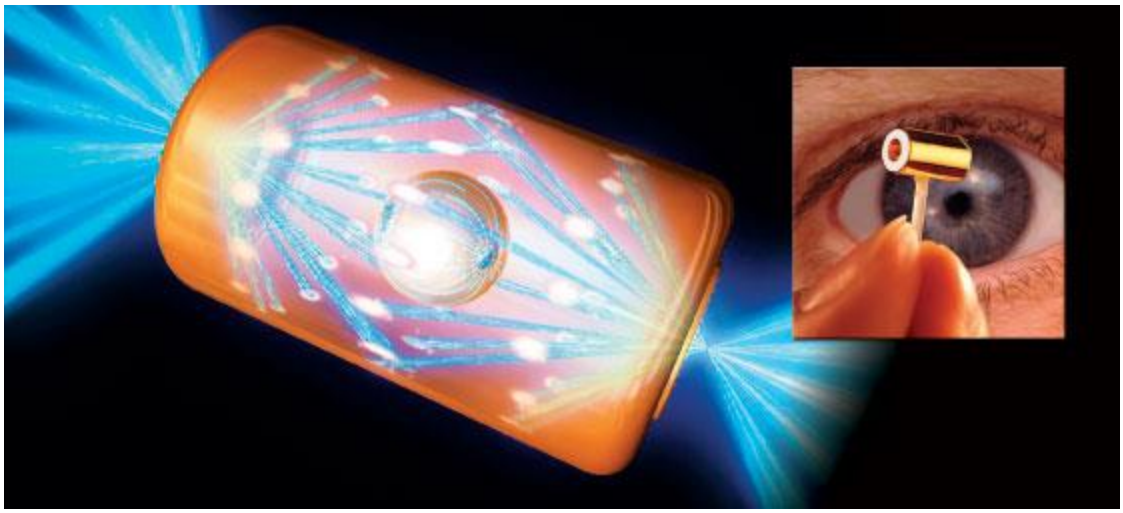

Figure 9: An artist's rendition of a hohlraum, used for indirect drive inertial confinement fusion. Laser beams are directed through the holes on either end of the hohlraum and impact upon the sides, creating x-rays, which in turn compress the fuel pellet. The inset image shows the size of the hohlraum compared to the human eye, for scale.

1.2 Fusion Reactions

In order to develop a diagnostic for inertial confinement fusion, it is important to understand the various nuclear reactions that can occur. There are a number of possible fusion reactions between deuterium and other light nuclei; among these are reactions between deuterium and tritium,

$$\mathrm{D} + \mathrm{T} \rightarrow \alpha + n + 19.6\ \mathrm{MeV}, \tag{5}$$

two deuterium nuclei,

$$\mathrm{D} + \mathrm{D} \rightarrow \begin{cases} p + \mathrm{T} + 4.1\ \mathrm{MeV} \\ n + {}^{3}\mathrm{He} + 3.2\ \mathrm{MeV}, \end{cases} \tag{6}$$

and deuterium and ^{3}He,

$$\mathrm{D} + {}^{3}\mathrm{He} \rightarrow p + \alpha + 18.3\ \mathrm{MeV}. \tag{7}$$

While all of these reactions are possible, the DT reaction has the largest cross section at low energies [8], and thus is the most readily achievable under laboratory conditions. In order to make use of this reaction, however, supplies of both deuterium and tritium are necessary. Deuterium is a naturally occurring isotope of hydrogen; however, tritium is not, and would need to be produced on site in order to make power generation feasible. Most plans for tritium production involve breeding it from lithium via the following reactions;

$$n + {}^{6}\mathrm{Li} \rightarrow \mathrm{T} + \alpha, \text{ and} \tag{8}$$

$$n + {}^{7}\mathrm{Li} \rightarrow \mathrm{T} + \alpha + n, \tag{9}$$

using neutrons produced by the primary fusion reaction, such as the reactions in Equations (5) or (6).

This paper is primarily focused on the development of a diagnostic for inertial confinement fusion at or near ignition. As all facilities capable of operating near this domain are currently using DT fusion reactions, we will now restrict our focus to the secondary reactions occurring within a cryogenic DT fuel pellet leading to the production of tertiary neutrons, shown in Figure 10.

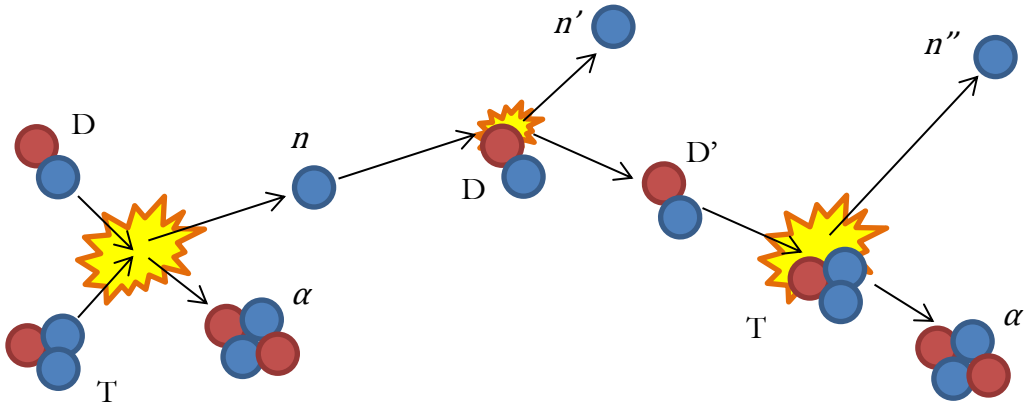

Figure 10: The reaction chain occurring in DT fusion leading to the production of tertiary neturons. A deuteron and a triton fuse into an alpha particle releasing a primary neutron (n). That neutron elastically scatters from another deuteron or triton creating a knock-on deuteron or triton and a secondary neutron (n'). The then knock-on undergoes a secondary fusion reaction creating a tertiary neutron (n").

In the primary fusion reaction, very low energy deuterons and tritons combine into alpha particles, releasing 14.1 MeV neutrons, known as primary neutrons:

$$\mathrm{D} + \mathrm{T} \rightarrow \alpha + n\ (14.1\ \mathrm{MeV}) \tag{10}$$

Some of the neutrons then elastically scatter off other deuterons or tritons in the fuel, creating knock-on ions (D', with energies up to 12.5 MeV, or T', with energies up to 10.6 MeV) and secondary neutrons (n', with the remainder of the energy):

$$n + \mathrm{D}\ (\mathrm{or}\ \mathrm{T}) \rightarrow n' + \mathrm{D}'\ (\mathrm{or}\ \mathrm{T}'). \tag{11}$$

There is then a chance that the knock-on ions will undergo a secondary fusion reaction, yielding even higher energy tertiary neutrons:

$$\mathrm{D}' + \mathrm{T}\ (\mathrm{or}\ \mathrm{D} + \mathrm{T}') \rightarrow \alpha + n''(12 - 30\ \mathrm{MeV}) \tag{12}$$

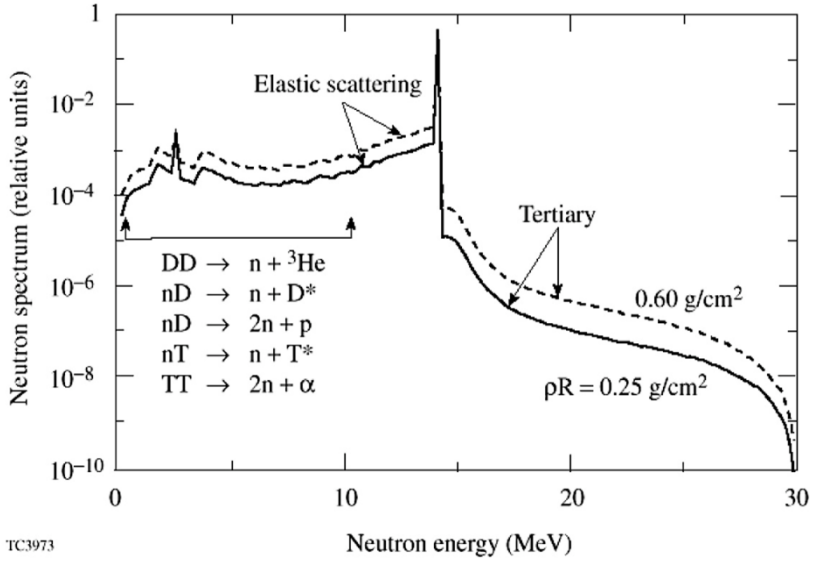

Figure 11: Calculated neutron yield for a compressed DT pellet for two values of the density-radius product ϱR. Neutrons with energies less than that of the primary neutrons can come from a variety of sources, including elastic scattering and other fusion reactions, while only tertiary neutrons have energies higher than that of the primary neutrons. Figure from Reference 20.

The tertiary neutrons are the only neutrons produced with an energy greater than the primary neutrons, as shown in Figure 11. As these neutrons are the only neutrons in this energy range, they can be detected separately from the primary neutrons via nuclear reactions with a high energy threshold, as discussed in Section 1.3.3, making them an ideal candidate to be used as a diagnostic probe for studying the reaction parameters.

1.3 ICF Diagnostics

An important quantity for characterizing an inertial confinement fusion reaction is the fraction of the fuel burned in the reaction, f_b,

$$f_b = \frac{N_{i,o} - N_{i,f}}{N_{i,o}} \tag{13}$$

where $N_{i,o}$ is the fuel ion density at the beginning of the burn and $N_{i,f}$ is the fuel ion density at the end of the burn. The burn fraction can be determined by measuring the product of the density ρ_b and radius R_b of the compressed fuel pellet at the point at which burn conditions are achieved:

$$\rho_b R_b \propto \frac{f_b}{1 - f_b} \tag{14}$$

We will therefore examine various ways to determine this ρR parameter in a DT inertial confinement fusion reaction.

1.3.1 Knock-On Ions

The likelihood that a primary neutron will strike an ion in the fuel is directly proportional to the mean value of ρR. As such, the ratio between the number of knock on ions and the primary neutron yield can be used to directly measure ρR [21]. The fact that the knock-ons are charged particles, however, causes them to lose energy as they progress outward through the fuel pellet. As a result, this diagnostic can only be used when ρR is small, as the spectrum is significantly distorted for ρR in excess of 100 mg/cm^2. Therefore, while this technique can be used for near-term experiments on the OMEGA

laser system (total target $\rho R \leq 200$ mg/cm^2), it cannot be used at the NIF (typical target $\rho R \sim 1$ g/cm^2) [20].

1.3.2 Elastically Scattered Neutrons

The elastically scattered neutrons are created at the same time as the knock-on ions, and as such can also be used to directly measure ρR much like the knock-on ions. Furthermore, they are neutral and therefore do not undergo the same spectrum degradation as the knock-ons. It has been calculated that while there are many sources of neutrons with energies less than 10 MeV, including the D(D,n)^{3}He, T(T,2n)α, and D(n,2n)p reactions, as shown in Figure 11, the only source of neutrons in the range of 10 MeV to 14 MeV is elastic scattering [20]. Of concern to this diagnostic is the large number of primary neutrons created in the reaction. It is possible to identify the neutrons with energies lower than 14 MeV, however the primary neutrons could elastically scatter off of materials which are near the detector and fall into this energy range.

1.3.3 Tertiary Neutrons

Tertiary neutrons are produced when a knock-on ion undergoes a second fusion reaction with another ion in the fuel pellet, leading to an overall abundance proportional to $(\rho R)^2$. While these neutrons are therefore produced much less frequently than the secondary neutrons and knock-ons, the total tertiary neutron yield at the NIF is expected to be large enough to use. Using multiple detectors at various angles around the fuel pellet can also be used to determine the angular dependence of ρR as well as its average value, allowing hydrodynamic instabilities in the fuel pellet to be detected [22].

The simplest method of detecting these tertiary neutrons is via activation reactions with high thresholds, such as the ^{12}C(n,2n)^{11}C reaction studied in this paper. The activation threshold for the ^{12}C(n,2n) reaction, E_{th}, is given as 20.2 MeV by Brolley Jr. et al. [23]; neutrons with energies greater than this will activate the carbon, while neutrons below the threshold will not. The number of tertiary neutrons can thus be determined by counting the number of ^{11}C beta decays via gamma rays from positron annihilation, as shown in Figure 12 . Tertiary neutrons can react with a high-purity ^{12}C target placed in the reaction chamber, thereby activating it:

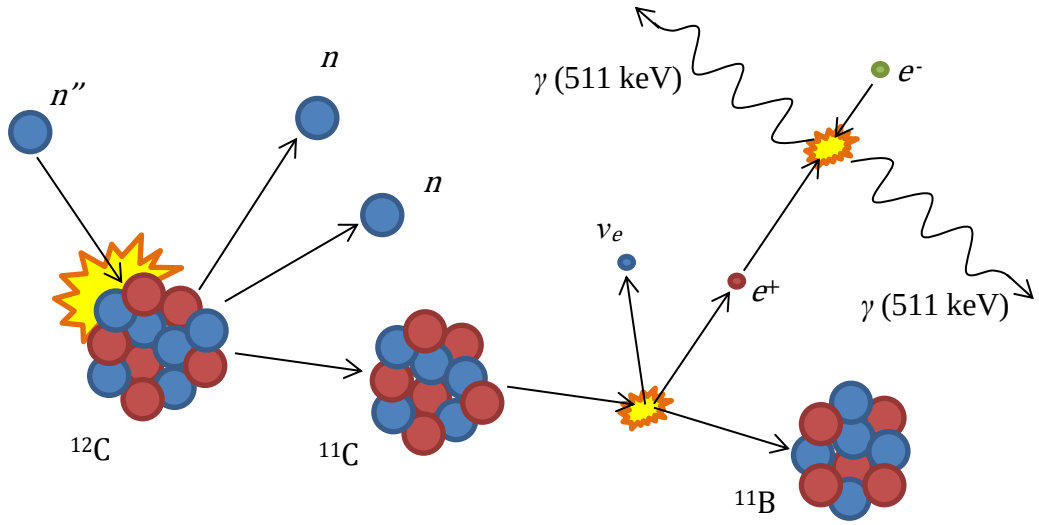

Figure 12: The activation and subsequent decay process of ^{12}C. An incoming tertiary neutron activates the 12C nucleus. The newly formed ^{11}C then beta decays into ^{11}B with a half-life of 20.334 minutes. The emitted positron then annihilates with an atomic electron, resulting in back-to-back 511 keV gamma rays.

$$n'' + {}^{12}\mathrm{C} \rightarrow 2n + {}^{11}\mathrm{C}. \tag{15}$$

The ^{11}C then undergoes β+ decay into ^{11}B with a half-life of 20.334 minutes:

$${}^{11}\mathrm{C} \rightarrow {}^{11}\mathrm{B} + \nu_e + e^+. \tag{16}$$

The positron is almost immediately annihilated, producing back-to-back 511 keV gamma rays. It is important that the ^{12}C sample be of high-purity (>99.999%) due to the large abundance of primary neutrons. The number of primary neutrons hitting the target is many orders of magnitude greater than the number of tertiary neutrons, as shown in Figure 11, so the presence of any impurities with a lower activation threshold would cause the signal from the tertiary neutrons to be swamped.

As this diagnostic tool does not involve sensitive detectors, which could be damaged by the high neutron flux at ignition, and additionally yields data about the instability of the fuel under compression, it may be used at the NIF in the near future. However, the lack of agreement between previous measurements of the $^{12}C(n,2n)^{11}C$ cross-section, shown in Figure 13, currently prevents its

implementation. While a number of measurements have been made previously, these measurements disagree in the energy region of interest. The experiment described in this paper is an attempt to perform a more accurate measurement of this cross-section, improving upon the techniques of previous work.

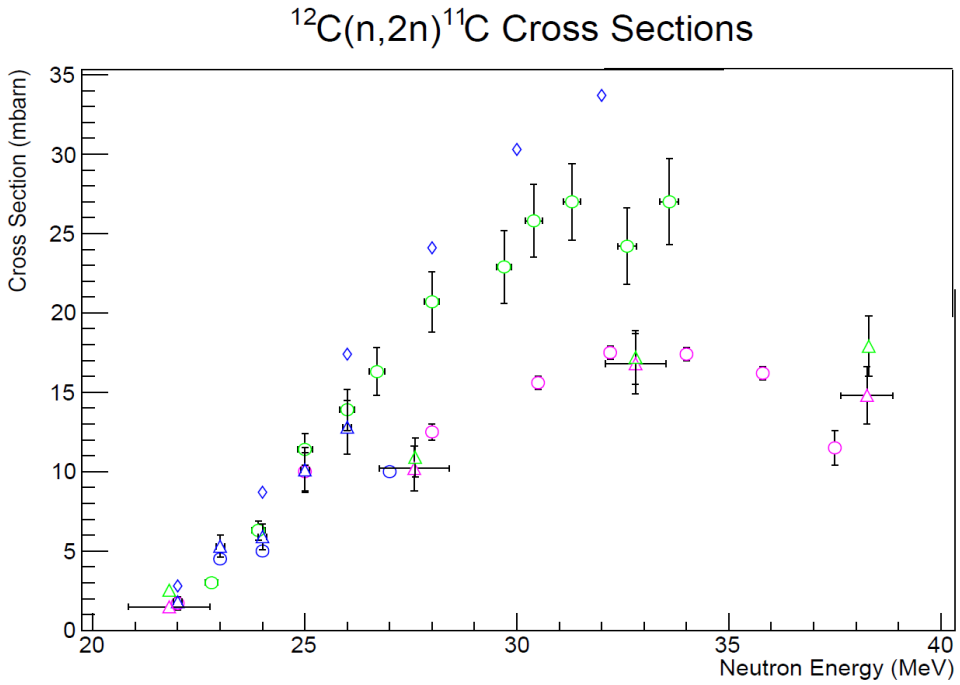

Figure 13: Published cross-sections for the $^{12}C(n,2n)^{11}C$ reaction Blue circles are from Brolley et al. [23], pink circles from Brill et al. [24], green circles from Anders et al. [25], blue triangles from Welch et al [26]., pink triangles from Soewarsono et al. [27], green triangles from Uno et al. [28], and blue diamonds from Dimbylow [29]. These measurements disagree by as much as a factor of two in the range of 20 to 30 MeV, the energy range of tertiary neutrons.

Chapter 2

TECHNIQUES FOR MEASURING THE $^{12}C(n,2n)^{11}C$ CROSS-SECTION

An accurate measurement of the $^{12}C(n,2n)^{11}C$ cross-section needs to be performed before the ICF diagnostic described in Section 1.3.3 can be implemented. Various measurements and calculations of this cross-section have been performed, but they disagree with each other in the energy range of tertiary neutrons. Therefore, an experiment has been performed to improve upon these prior measurements.

The total cross-section of a reaction is a value proportional to the likelihood of the reaction occurring and has units of area (typically mbarn). In the case of an monoenergetic particle beam interacting with a solid target, the differential cross section, σ, with units of area/solid angle is given by

$$dN_s = \sigma(\theta, E)FAN d\Omega, \tag{17}$$

where F is the flux of incoming particles with energy E, in units of number of particles per unit area per unit time, N and A are the areal number density and area, respectively, of the target spot, and dN_s is the number of particles scattered per unit time at an angle of θ into the solid angle $d\Omega$.

The name cross-section is used for this quantity because in certain cases the cross-section is almost the same as the physical cross-section of the particle. Cross-sections are generally measured in units of barns, with 1 barn equaling 10^{-24} cm^2. This unit originated as a result of experiments on uranium while developing the atomic (fission) bomb; the measured value of the uranium fission cross-section was much larger than expected, causing the researchers to remark that it was "as big as a barn."

2.1 Previous Measurements and Calculations

There have been a number of previous attempts to determine the $^{12}C(n,2n)^{11}C$ cross-section, both experimentally and using statistical models based on empirical data. Unfortunately, these published

values disagree in the energy range of the tertiary neutrons for use as an ICF diagnostic, as shown in Figure 13. An analysis of each previous experiment follows.

2.1.1 J. E. Brolley Jr., J. L. Fowler, and L. K. Schlacks. (1952) [23]

Neutrons were produced via the T(d,n)α reaction by bombarding tritium gas with 10.5 MeV deuterons accelerated by the 42 in cyclotron at Los Alamos. The carbon targets, in the form of polyethylene foils about 11 mg/cm^2 thick, were supported in such a way as to minimize additional material near the target, as shown in Figure 14. Rectangular foils of 2.54 cm × 5.08 cm were folded into a 2.54 cm square and suspended at a distance of approximately 15 cm from the tritium target. Neutron energy was varied by adjusting the angle of the foil relative to the beam line. The activated rectangular foils were then counted using a set of three glass-walled Geiger counters.

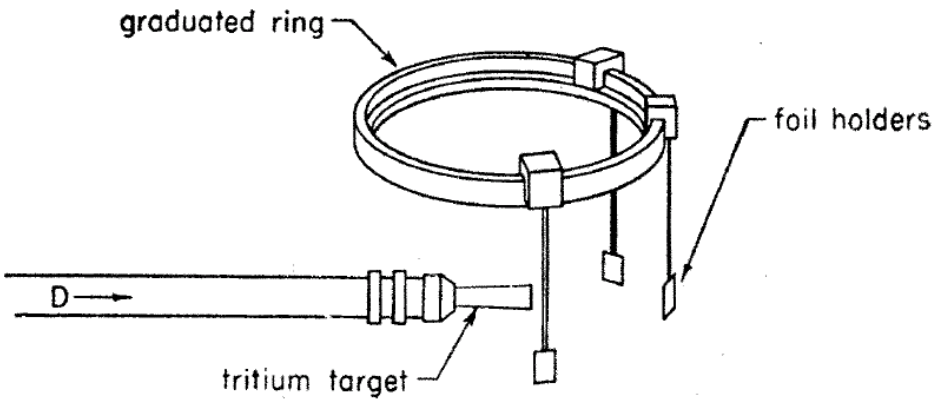

Figure 14: The activation setup as used by Brolley Jr. et al. Deuterons, with energy of 10.5 MeV, were accelerated into a gaseous tritium target, producing neutrons via the T(d,n)α reaction. Rectangular carbon foils were suspended at a distance of around 15 cm using a graduated ring centered above the tritium. Figure taken from Reference 23.

Efficiency calibration of the Geiger counters was performed relative to end-window counters, which were themselves calibrated against a RaD+E standard. To perform this calibration, additional 2.54 cm × 5.08 cm polyethylene foils were folded and placed between two circular foils 1.43 cm in diameter and fastened directly to the end of the target cell. The circular foils were counted on the end-window counters and the rectangular foils on the Geiger counter. This allowed the Geiger counters to be

calibrated relative to the end-window-counters, which have a known efficiency as given by the RaD+E standard. [23].

2.1.2 O. D. Brill, N. A. Vlasov, S. P. Kalinin, and L. S. Sokolov. (1961) [24]

Neutrons were produced via the T(d,n)α reaction by bombarding a solid tritium and zirconium target with 20 MeV deuterons accelerated the cyclotron of the Atomic Energy Institute, Academy of Sciences of the USSR. Neutron energy was varied by slowing the deuterons with platinum foils placed directly upstream of the tritium target. A graphite target of unspecified dimensions was irradiated at an angle of 0°, with target activity then being measured with a Geiger counter. The absolute sensitivity of the counter was determined via measurement of the γ activity of a ^{198}Au sample with known β activity. The sensitivity of the γ detector to 0.511 MeV annihilation γ rays and to the 0.411 MeV γ rays from ^{198}Au was assumed to be the same [24].

2.1.3 P. J. Dimbylow (1980) [29]

A theoretical calculation for the cross-section was performed using a nuclear optical model, in which various nuclear models are analogous to the scattering and absorption of light. In the optical model, the nucleus is assigned a complex optical potential, which provides a macroscopic refractive index for the nucleons. Elastic scattering is described by the real part of the potential and inelastic processes are described by the imaginary part. This potential was fit to give total cross-sections at 20 MeV and 50 MeV that agree with prior measurements, and then used to predict the total elastic and inelastic cross-sections.

The cross-sections for individual reactions were calculated based on a statistical model of level densities, which describe the formation and decay of a compound nucleus. The nucleus was assumed to behave as a Fermi gas composed of neutrons and protons with equidistant and non-degenerate single particle levels. Emission probabilities of various particles were calculated for reaction chains of up to six sequential decays. The level density parameters were fit to known reaction data and used to predict the cross-sections for those reactions with no prior measurements [29].

2.1.4 B. Anders, P. Herges, and W. Scobel (1981) [25]

Neutrons were produced via the T(d,n)α reaction by bombarding a tritium-absorbed titanium foil with 7 – 16 MeV deuterons using the Hamburg Isochronous Cyclotron. A target of natural carbon with a diameter of 22 mm and unspecified thickness was placed at 0° at a distance of 40 mm from the tritium. The target was irradiated for 1 hour, and the neutron flux was determined via a recoil proton detector, consisting of a 1" diameter × 1.5" thick stilbene crystal mounted on a 56 AVP multiplier, placed at 0°. The target activation was measured using two 3" diameter × 3" thick NaI detectors in coincidence, with the efficiency determined via Monte-Carlo simulations and checked with a calibrated ^{22}Na source [25].

2.1.5 P. Welch, J. Johnson, G. Randers-Pehrson, and J. Rapaport (1981) [26]

Neutrons were produced via the T(d,n)α reaction using the tandem van de Graaff accelerator at Ohio University. A 1.77 cm diameter × 1 cm thick target of natural graphite was activated, and the gamma activity was counted using an 80 cm^3 germanium-lithium detector calibrated with a NaCl sample [26].

2.1.6 T. S. Soewarsono, Y. Uwamino, and T. Nakamura (1992) [26]

Neutrons were produced via the ^{7}Li(p,n)^{7}Be reaction by bombarding a 2 mm thick solid ^{7}Li target backed with 12 mm of graphite with protons in the energy range of 20 – 40 MeV. This reaction creates a neutron spectrum with a peak of high-energy neutrons having a full-width at half-maximum of 1.4 – 2.3 MeV, depending on the proton energy. This reaction also produces a large number of lower energy neutrons.

Experiments were performed with both the graphite-backed lithium as well as just graphite for a background run. A natural sample of carbon was placed at a distance of 10 cm from the lithium target. The gamma activity of each sample was counted using a high-purity germanium detector calibrated with several standard gamma-ray sources.

The neutron spectrum was determined separately using a 127 mm diameter by 127 mm long NE-213 scintillation detector at a distance of 10 m from the lithium target. As during activation, experiments

were performed with both graphite-backed lithium and graphite alone as a background. The effects of the low-energy neutron tail above the threshold were accounted for using cross-sections based upon prior literature and measurements at lower energies [26].

2.1.7 Y. Uno, Y. Uwamino, T. S. Soewarsono, and T. Nakamura. (1996) [28]

Neutrons were produced via the ^{7}Li(p,n)^{7}Be reaction by bombarding a lithium target with a beam of protons, with energies in the range of 20 – 40 MeV. A sample of natural carbon with a thickness of 3 mm and diameter of 20 mm was placed 10 cm in front of the neutron source and irradiated for 10 min. A measurement of the ^{7}Be produced in the lithium target was used to determine the absolute neutron fluence, with the beam current of the proton beam recorded to monitor fluctuations in the beam. The gamma rays emitted by the activated samples were measured using two high-purity germanium detectors. The effects of the low energy neutron tail in the region above the threshold were accounted for using cross-sections based upon prior literature and the measurements at lower energies [28].

2.2 Measurement Techniques

All of the previous experiments used the activation technique, measuring the decay rate of the produced ^{11}C into ^{11}B. For our experiment, a number of other techniques for determining the ^{12}C(n,2n)^{11}C cross-section were considered. Among these were measurements of prompt de-excitation gamma rays, detection of the scattered neutrons, detection of the recoil ^{11}C nuclei, and the previously used activation technique. Of these techniques, it was determined that only activation was feasible with the available resources.

2.2.1 Prompt Gamma Rays

One method considered was to measure the prompt de-excitation gamma rays resulting from the ^{12}C(n,2n)^{11}C reaction. This reaction often leaves the ^{11}C nuclei in an excited state, producing gamma rays upon de-excitation. This technique has been used before to measure the cross-sections for other reactions [30]. A proposed experiment, shown in Figure 15, was designed to be performed at the Los

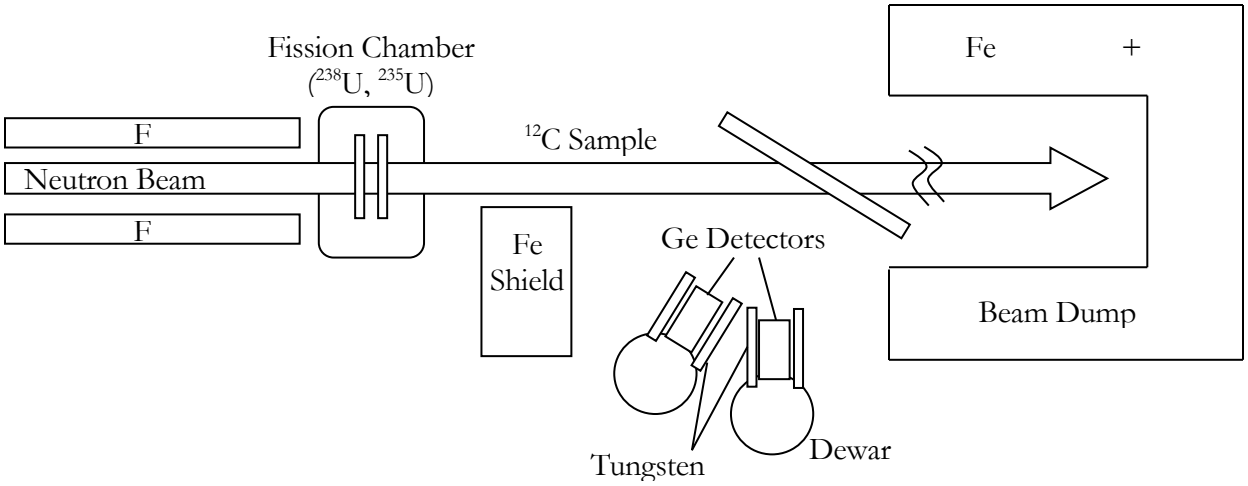

Figure 15: A proposed experimental setup to measure prompt de-excitation gamma rays resulting from the ^{12}C(n,2n)^{11}C reaction. The neutron beam is first allowed to pass through a fission chamber, which would measure the energy dependence of the beam flux, before being allowed to hit the ^{12}C sample. The de-excitation gamma rays would then be detected by high-resolution germanium detectors placed at a backward scattering angle.

Alamos Neutron Science Center (LANSCE), which can produce well-collimated pulsed neutron beams at energies up to 800 MeV.

The high-energy neutron beam would be allowed to pass through a fission chamber, in which the energy dependence of the beam flux would be determined, before striking the ^{12}C target. De-excitation gamma rays would then be counted using high-resolution germanium detectors placed at backwards

scattering angles. The time-of-flight of incident neutrons would be used to determine the energy of the incident neutrons on an event-by-event basis.

While this method has been highly successful for even-even residual nuclei [30], in which direct transitions to the 0+ ground states are strongly inhibited, for an odd-even residual nucleus such as ^{11}C a significant number of reactions may leave the nucleus in its ground state. The fraction of nuclei for which this is the case is not known, allowing only partial production cross sections to be measured and requiring the use of nuclear model calculations to determine the total cross section.

Flux (4FP15R) (20-30 MeV)	45000 neutrons/sec/MeV
Cross section (25 MeV)	0.007 b
Detector Absolute Efficiency at 2 MeV (50% Rel Eff HPGE, ~200 cc)	1.3×10^{-3}
Detector Absolute Efficiency at 4 MeV (50% Rel Eff HPGE, ~200 cc)	8×10^{-4}
Distance to detector	14 cm
Target (graphite)	5 mm thick
Count rate @ 2 MeV (assume 1/3 of total decays)	80 counts/hour/MeV
Count rate @ 4MeV (assume 1/3 of total decays)	50 counts/hour/MeV

Table 1: Experimental parameters and count rate estimate for the prompt gamma technique.

2.2.2 Outgoing Neutron Detection

Another proposed method was to detect both outgoing neutrons produced by the $^{12}C(n,2n)^{11}C$ reaction. In this experiment, also to be performed at LANSCE, the neutron beam would be allowed to strike a series of plastic scintillator active targets, as shown in Figure 16. These active targets would be used to detect the recoil nucleus and determine the incident neutron energy via time-of-flight information. Surrounding the target are eighteen large plastic scintillator bars, each 2 m high x 10 cm x 10 cm, which would be used to detect the outgoing neutrons.

This measurement method has an advantage over the other methods as it would allow for the simultaneous measurement of the cross-section as a function of neutron scattering angle and energy for all incident neutron energies from threshold to several hundred MeV. It was determined to be infeasible, however, as the size and number of detectors and time required would make this technique very expensive to implement.

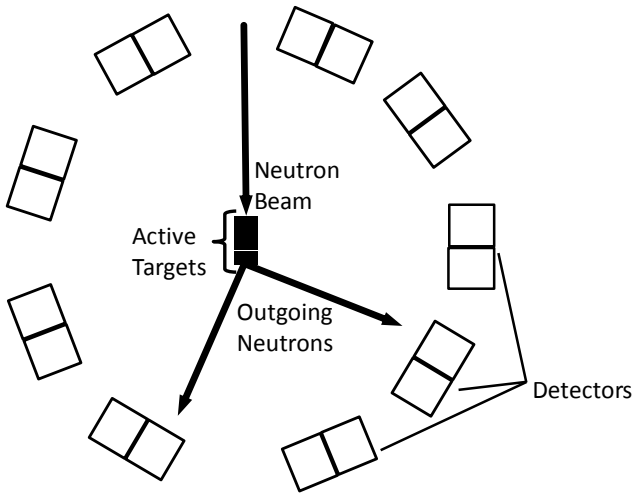

Figure 16: Proposed experimental setup to measure both outgoing neutrons resulting from the $^{12}C(n,2n)^{11}C$ reaction. The neutron beam would be allowed to strike a series of active plastic scintillator targets, which would detect the recoil nucleus and incident neutron energy. Eighteen large plastic scintillators surrounding the target would then detect the outgoing neutrons.

Flux (4FP15R) (20-30 MeV)	45000 neutrons/sec/MeV
Cross section (0.007/4π/4π) b/sr^2 @ 25 MeV)	44 μb/sr^2
Detector (two 2 m × 10 cm × 10 cm plastic)	0.28 Sr
Angles	9
Target (ten BC418 active targets)	10 x 2 mm thick
Count rate	25 counts/pair/day/2 MeV

Table 2: Experimental parameters and count rate estimate for the outgoing neutron technique.

2.2.3 Recoil ^{11}C Nuclei

A third proposed method was to identify and count the recoiling ^{11}C nuclei. In this method, a well-collimated neutron beam, such as is available at LANSCE, would be allowed to strike a thin graphite target, from which the produced ions could escape. These ions could then be detected and identified using a focusing magnetic spectrometer. The energies of the incident neutrons could be determined

event-by-event using time-of-flight techniques. By detecting the produced ions, this technique would have the advantage of allowing many different reactions to be measured simultaneously and also allowing the ion angular distributions to be determined. Unfortunately, the short range of ions travelling in the target (a 10 MeV ^{11}C nucleus has a range of around 7 μm in graphite) would require an extremely thin target, thus causing the count rate to be prohibitively low. Measuring over a larger detector solid angle would increase the count rate but prevent identification of the ions, as the ions would then have wildly different flight paths through the spectrometer.

Flux (4FP15R) (20-30 MeV)	45000 neutrons/sec/MeV
Detector	25 msr
Cross section (0.007/4π b/sr @ 25 MeV)	0.56 mb
Target	0.15 μm graphite foil
Count rate	0.1 counts/day/MeV

Table 3: Experimental parameters and count rate estimate for the recoil ion technique.

2.2.4 Activation

The final measurement technique considered was the activation method similar to that performed in previous measurements. In this technique, monoenergetic neutrons would strike graphite and polyethylene targets. As the ^{11}C nucleus undergoes β^+ decay with a half-life of around 20 minutes, the total number of ^{11}C nuclei created could be determined afterwards by measuring the time dependance of the decay spectrum. The incident neutron flux could be measured during activation, either directly or via elastically scattered protons from the polyethylene target.

Of the considered measurement techniques, only the activation technique was determined to be feasible. Using the tandem van der Graaff accelerator at Ohio University, deuterons would be accelerated at a titanium tritide target, producing monoenergetic neutrons via the T(d,n)α reaction. A design study was performed for 24 MeV neutrons, using a neutron flux of 10^7 neutrons/s hitting a 1

mm thick CH_2 target with a density of 0.89 g/cm^3, with protons being scattered into a silicon detector with an area of 1 cm^2 placed at a distance of 10 cm behind the CH_2 target, for a solid angle of 10 msr. The cross-section of the $^{12}C(n,2n)$ reaction was assumed to be 5 mb and the cross-section for np scattering was assumed to be 33 mb/sr. These parameters gave an estimated ^{11}C activity of 190 Bq after 2 hours of activation, and a recoil proton count rate of 13 counts/s. The actual setup was based upon this design study and is described in Section 3.1.

After activation, the targets would be removed to a separate room for decay counting. Decay of the ^{11}C nucleus yields a positron, which, upon annihilation, releases two back-to-back gamma rays at 511 keV. These gamma rays were measured via two NaI detectors in coincidence, allowing the time spectrum of the decay to be determined. From this decay spectrum, the number of ^{11}C nuclei present in the target immediately after activation would be determined. The actual setup and procedure used for counting these ^{11}C decays is described in Section 3.2.

Flux (Ohio Univ. 24 MeV, 2 cm from tritium cell)	10^7 neutrons/sec
Cross section for $^{12}C(n,2n)$ (24 MeV)	5 mb
Cross section for np scattering at 0° (24 MeV)	33 mb/sr
Silicon Detector (1 cm^2 at 10 cm from CH2)	10 msr
Target (CH2 0.89 g/cm^3)	1 mm thickness
^{11}C activity from (n,2n) in CH2 target after 2 h	190 Bq
Recoil proton count rate	13 counts/sec

Table 4: Experimental parameters and count rate estimate for the activation technique.

This current experiment is an improvement on previous measurements in a variety of ways. First, the neutron source was highly monoenergetic. While other experiments generated their neutrons via the T(d,n)α reaction, most used cyclotrons which could only produce one energy of deuterons, often with

a relatively large energy spread. To achieve neutrons of lower energies, either the deuterons were slowed down in various substances or the neutron angle from the DT reaction was changed from 0°. Both of these techniques result in a broadening of the neutron energy spectrum. In our experiment, the deuteron energy in the Van de Graaff accelerator was adjusted, thus giving a monoenergetic neutron spectrum.

A second improvement was in the determination of the neutron flux. In our experiment, the neutron flux was determined indirectly via elastically scattered protons. These protons were then detected in a E-ΔE detector, allowing for the accurate identification of the recoil protons. The manner in which energy is distributed between the two detectors allows incoming charged particles to be identified by both energy and species. The polyethylene target used as the source of the recoil protons was also counted for activation. By using the same target to determine both the carbon activation rate and the neutron flux, the cross-section can be calculated with reduced systematic uncertainty. While other experiments have used recoil protons to determine the neutron flux, they were unable to identify the protons from background particles, nor did they use the proton source as an activation target.

A third improvement was the measurement of the carbon activation using back-to-back gamma detectors in coincidence. By only measuring the events that occurred in coincidence, we could isolate the gamma rays from positron annihilation in the carbon targets from background 511 keV gamma rays. Using NaI detectors for this measurement also allowed us to isolate the 511 keV gamma peak, which cannot be done using a Geiger counter as done in other experiments.

The final improvement is our careful measurement of the efficiency of the NaI detectors, described in Section 3.2. Experiments to measure this efficiency are being performed and used to validate a Monte-Carlo simulation. Some of the previous experiments used NaI detectors, but did not carefully verify their detector efficiency.

Chapter 3

EXPERIMENT

An experiment to measure the $^{12}C(n,2n)^{11}C$ cross-section in the energy range of 20-27 MeV was performed using the 4.5 MeV tandem van der Graaff accelerator at Ohio University. As described in Section 2.2.4, this experiment was designed to improve upon the prior measurements of this cross section, with a goal of achieving less than 5% uncertainty.

3.1 Activation

3.1.1 Apparatus

In our activation setup, shown in Figure 17 and Figure 18, deuterons were accelerated to energies between 3.07 MeV and 9.07 MeV and allowed to strike a titanium tritide target affixed to the end of the beam line. The end of the beam line was moved in a circular path by a "wobbler" to prevent any one place in the target from overheating and releasing the tritium. The beam, with a current of approximately 1.0 μA, was kept defocused by a pair of quadrupole magnets located 275 cm and 315 cm upstream of the target, and allowed to pass through a 1.27 cm diameter collimator located 45 cm upstream of the target. This ensured that the beam spot was spread out to prevent overheating, was uniform, and always struck the tritium target at the same location.

An optical bench was used to hold the targets and detectors in fixed positions at an angle of 0° with respect to the beam line, as shown in Figure 18. Neutrons leaving the tritium target were allowed to strike targets of high-density polyethylene and high-purity graphite. The polyethylene target was 1.64 mm thick and 2.54 cm in diameter, held in an aluminum ring, and placed with its front face at a distance of 7.0 cm from the tritium target. The graphite target was composed of three separate disks, with thicknesses of 1.28 mm, 2.57 mm, and 0.89 cm, given in order of increasing distance from the tritium target, each 7.62 cm in diameter with a 17.46 mm hole drilled through the center. These disks were placed with the front face at a distance of 14.0 cm from the tritium target. The two thinner

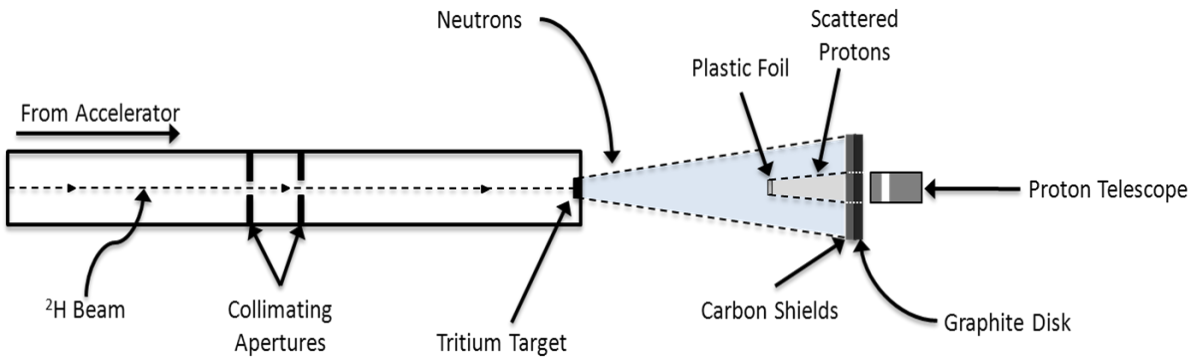

Figure 17: A schematic diagram of the activation apparatus used at Ohio University. Monoenergetic neutrons were produced via the T(d,n)α reaction by bombarding a solid tritium tritide with deuterons from the tandem van der Graaff accelerator. These neutrons were allowed to strike targets of both polyethylene and high-purity graphite. Elastically scattered protons from the polyethylene target were measured in a E-ΔE detector to determine the neutron flux.

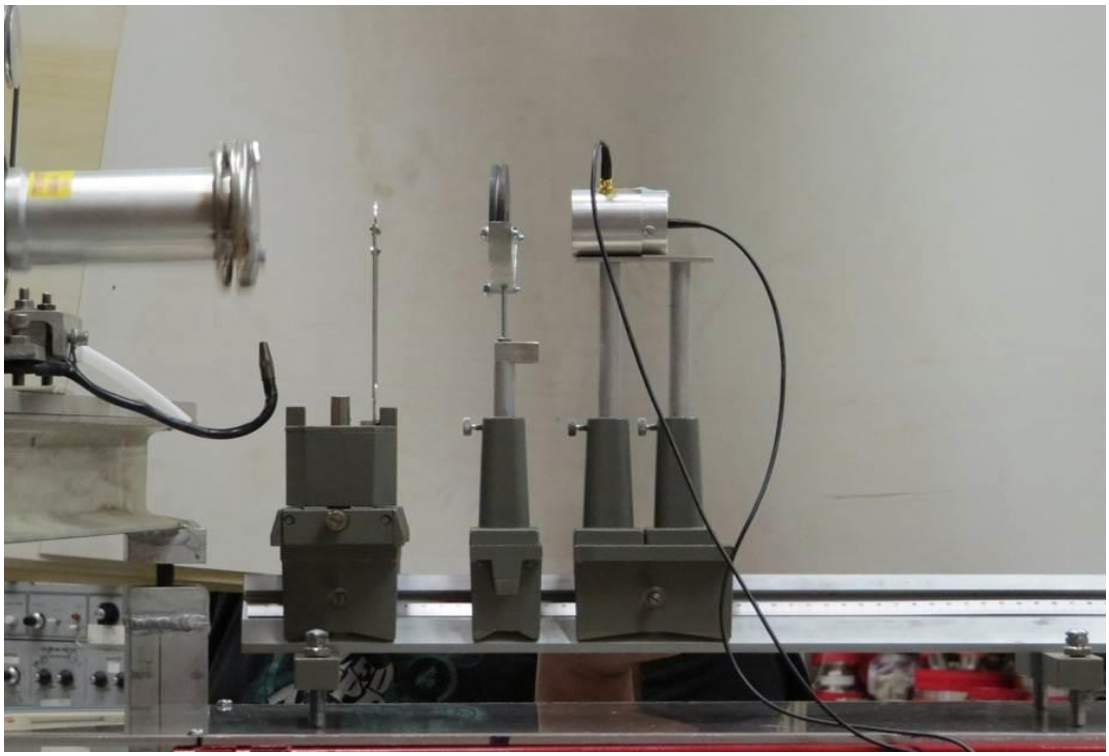

Figure 18: The activation setup as used at Ohio University. The targets and detectors (left-to-right: the polyethylene target, the graphite target, the E-ΔE proton telescope) were positioned along the beam line with aluminum supports attached to an optical bench. The targets and detector were aligned with the beam line using a theodolite.

graphite disks were originally meant to shield the thicker disk from recoil protons from the CH_2 target, but it was found that this shielding was unnecessary.

3.1.2 E-ΔE Proton Telescope

A proton telescope, consisting of a 300 μm thick, 150 mm^2 ion-implanted silicon ΔE detector and a 5000 μm thick, 200 mm^2 drifted-lithium silicon E detector, shown in Figure 19, was placed with the front of the detector casing at a distance of 18.0 cm from the tritium target in order to measure the protons emitted from the polyethylene via np-elastic scattering. The entrance to the ΔE detector was covered by a 5 μm thick aluminum foil to keep ambient light from entering, with the entire detector assembly housed in an aluminum casing. Detector pre-amplifiers, amplifiers, and bias voltage supplies

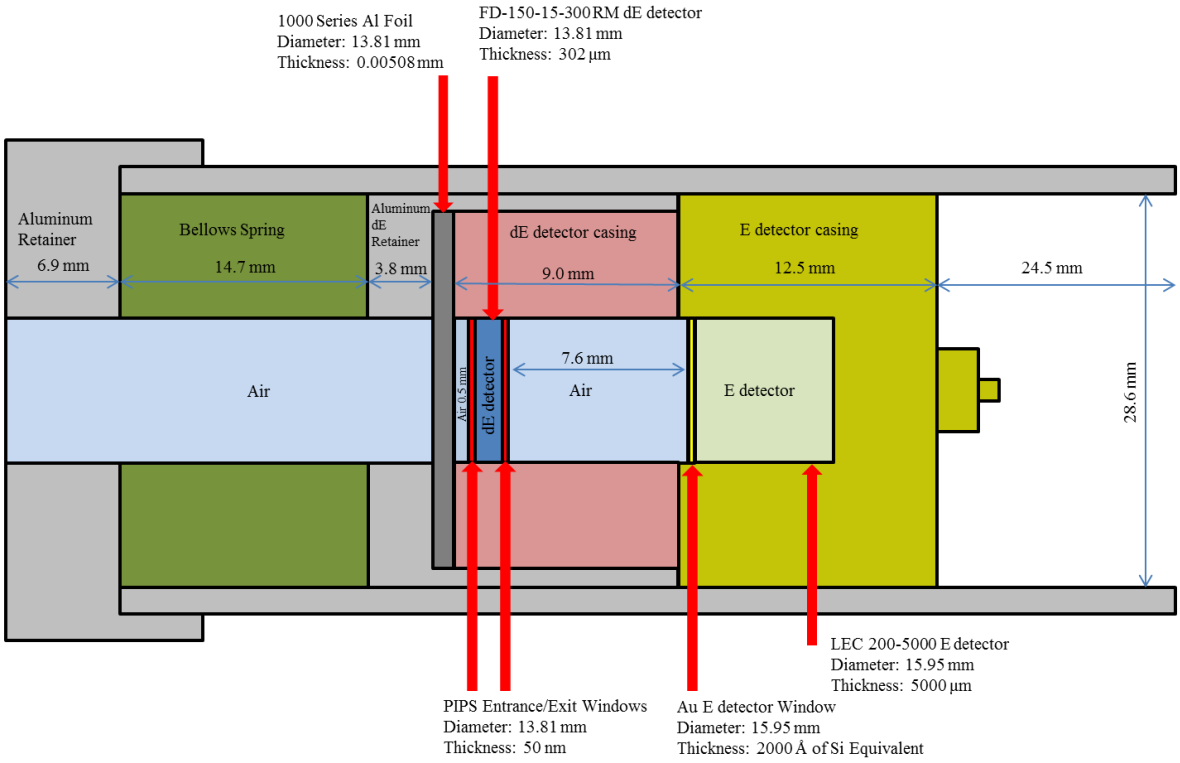

Figure 19: A schematic diagram of the E-ΔE proton telescope. The detector consists of a 300 μm thick, 150 mm^2 ion-implanted silicon ΔE detector followed by a 5000 μm thick, 200 mm^2 drifted-lithium silicon E detector held in an aluminum casing. The entrance of the ΔE detector was covered by a 5 μm thick aluminum foil to keep ambient light from entering the detector.

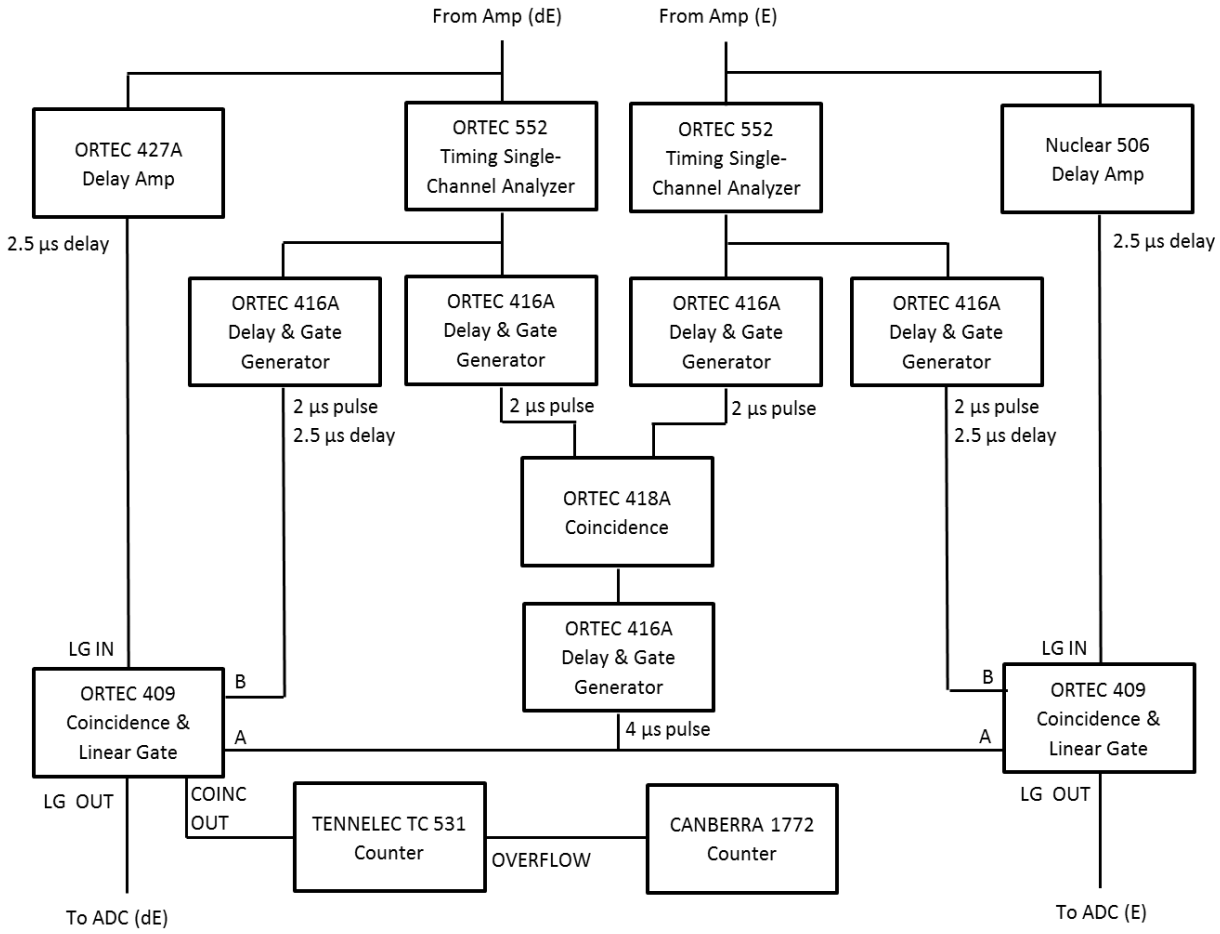

Figure 20: The circuit used for hardware coincidence detection and counting. Pulses from the amplifiers of the ΔE and E detectors enter the circuit, and are gated and tested for coincidence. Only those pulses which occurred in coincidence were sent onward to the MPA system for digitization. The number of coincidences was also counted in hardware using two cascading visual counters, allowing the dead time given by the MPA digitizer to be checked.

were located near the detectors, with the amplified signals being routed to the control room for additional processing and digitization.

Pulses from the amplifiers were sent to a hardware coincidence detection circuit, shown in Figure 20, with each pulse gated before being sent to a FastComTech MPA-3 multiparameter system, which digitized and recorded the pulse heights and timing. The number of pulses sent to the MPA system was also counted in hardware, allowing the dead time given by the MPA system to be checked.

The signal sent to the MPA system was the original pulse from the amplifier, gated on coincidence pulses. Two gate signals were created; a narrow gate on the pulse from the detector and a wide gate on coincidence events. Both signals were used with a linear gate to select which pulses to pass to the MPA system. The number of coincidences detected in hardware was counted using two cascading visual counters.

Two-dimensional histograms of the ΔE pulse heights versus the E pulse heights were generated, shown in Figure 21, allowing the events due to protons with the proper energy to be identified and counted. The integrated deuteron beam current was also recorded by the MPA system. For each run, this current was plotted over time, allowing major fluctuations in the deuteron beam to be detected.

Pulse-shape information from a neutron monitor, consisting of a 12.7 cm diameter liquid scintillator detector, were recorded separately. In order to identify the neutron pulses, a pulse shape analysis was performed, with the pulse rise time recorded by an Amptek ADMCA system. This information was used to ensure proper beam focus during activation, as described in Section 3.1.3, but not directly in the calculation of the cross-section.

3.1.3 Beam Focus

In order to ensure that the deuteron beam was centered with a relatively large beam spot, a number of short runs were performed after the beam was initially tuned. For each run, the ratio of the number of protons detected to the beam current and the ratio of the number of protons to the number of neutrons were both recorded. Over the course of these runs, each between 3 and 5 minutes long, the current in the final quadrupole magnet of the beam line was varied between 10.5 and 12.5 A. This current would shift the location of the beam spot slightly if the beam was off-center. If the variation in the measured count rates was more than 5%, it indicated that the beam spot had not originally been centered. In this case, the deuteron beam was re-tuned and this test was performed again.

The uniformity of the produced neutron beam and alignment of the targets and detector with the beam line were tested before the first activation run and after the final activation run. This was done by performing runs using special polyethylene targets which had been cut and monitoring the variation

of the produced protons. These targets consisted of a target from which the center was removed, the center of this target, and a target that had been cut in half. The half target was tested in various orientations, with any variation in the number of detected neutrons indicative of incorrect centering or an uneven neutron beam.

3.1.4 Activation Procedure

For each neutron energy, two runs were performed; the first to determine foreground proton count rate and activate the carbon targets, and the second to determine the background proton count rate. For the foreground run, all of the targets were present and irradiated for approximately 1.5 hr. The targets were then removed to be counted for activation, as described in Section 3.2, and the graphite disk was replaced with a dedicated disk used for background runs. For the background runs, only the graphite disk (without the shields) and aluminum retaining ring were in place; these were irradiated for approximately 0.5 hr.

3.2 Decay Counting

After the polyethylene target, graphite target, and graphite shields were activated, they were removed and counted separately using pairs of back-to-back 3" diameter × 3" thick NaI detectors, a detector being placed immediately adjacent to the face of each target, as shown in Figure 22. Pulses from these detectors were sent to a FastComTech MPA-4 multiparameter system, which digitized and recorded the pulse heights and timing. All three targets were counted simultaneously over a period of 2 hours (~6 ^{11}C half-lives).

For each target, the pulse heights for pulses in coincidence from each of the two detectors were used to make 2D histograms in order to select the 511 keV pulses in both detectors, as shown in Figure 23. These pulses are positron annihilation events caused by the beta decay of ^{11}C. The number of 511 keV coincidence events and the dead time of each detector were then determined as a function of time, and used to determine the abundance of ^{11}C in the target at the end of activation, as described in Section 4.3.

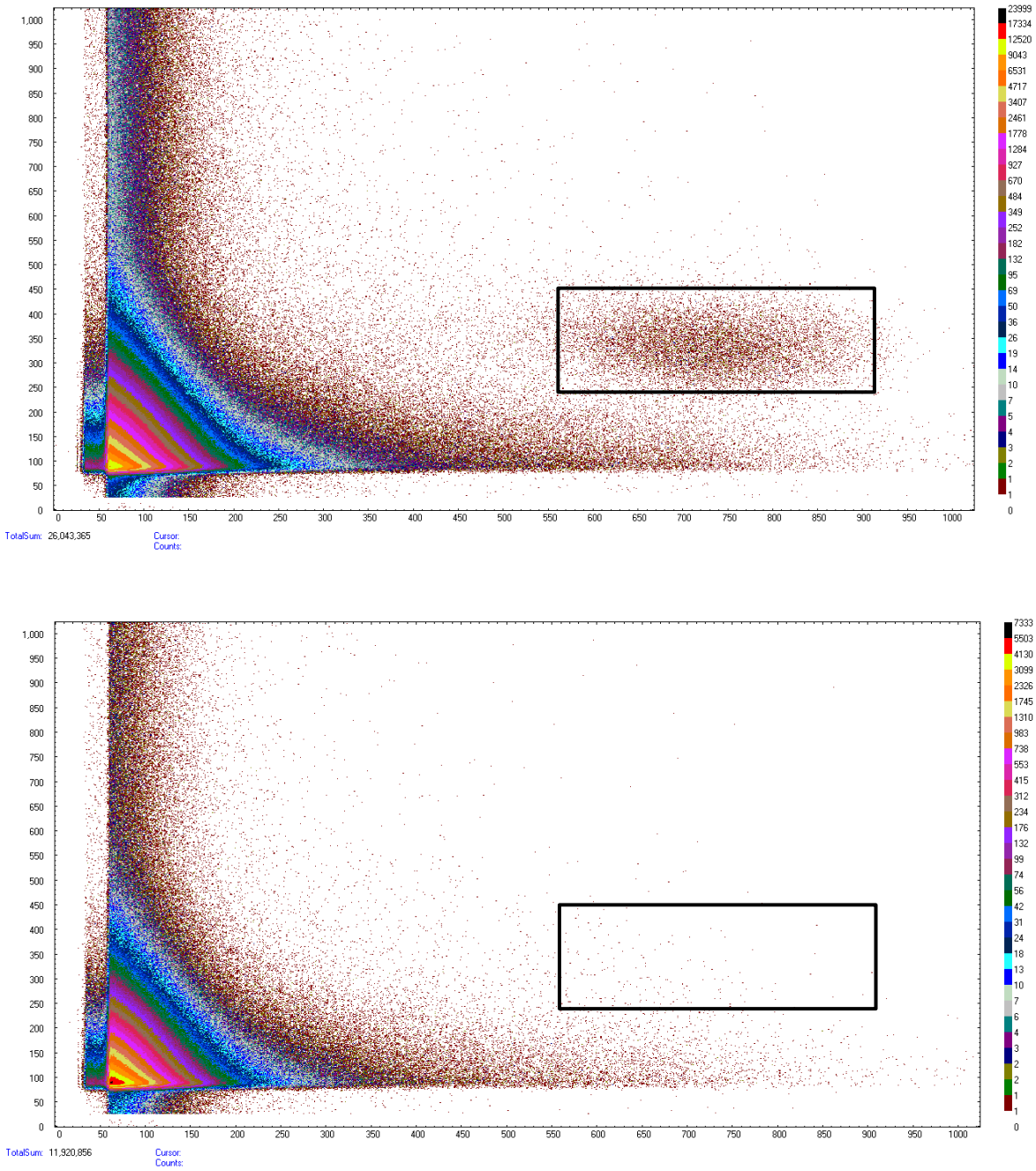

Figure 21: 2D histograms of the pulse heights from the ΔE and E detectors for a deuteron energy of 9.07 MeV. Plots for a foreground run with polyethylene target in place (top) and background run with the polyethylene removed (bottom) are shown. In both plots, the x-axis is the signal from the E detector and the y-axis the signal from the ΔE detector. The region used to count ~26 MeV protons can be seen in the boxed region at the lower right of the upper plot.

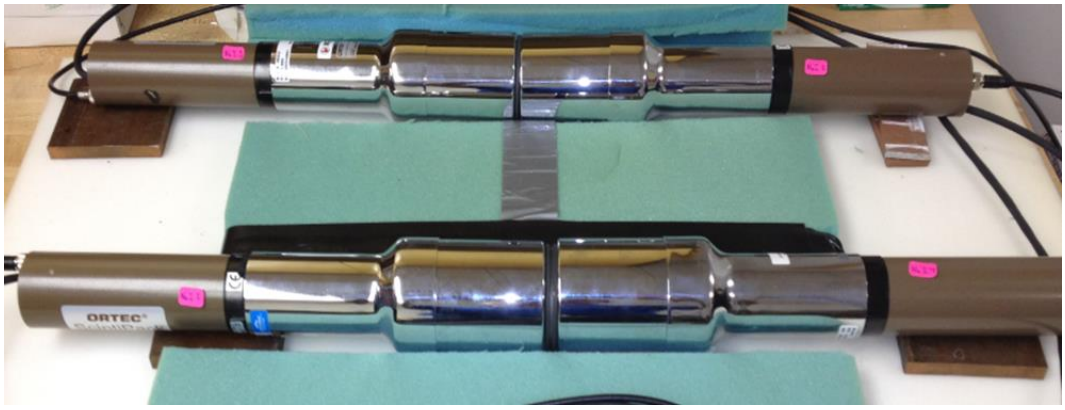

Figure 22: The NaI detectors used for measuring the activation of each target. A detector was placed immediately adjacent to either face of each target and counted for 2 hrs (~6 ^{11}C half-lives). The 511 keV pulses occurring in coincidence in each pair of detectors were determined as a function of time and used to determine the abundance of ^{11}C in the target immediately after activation.

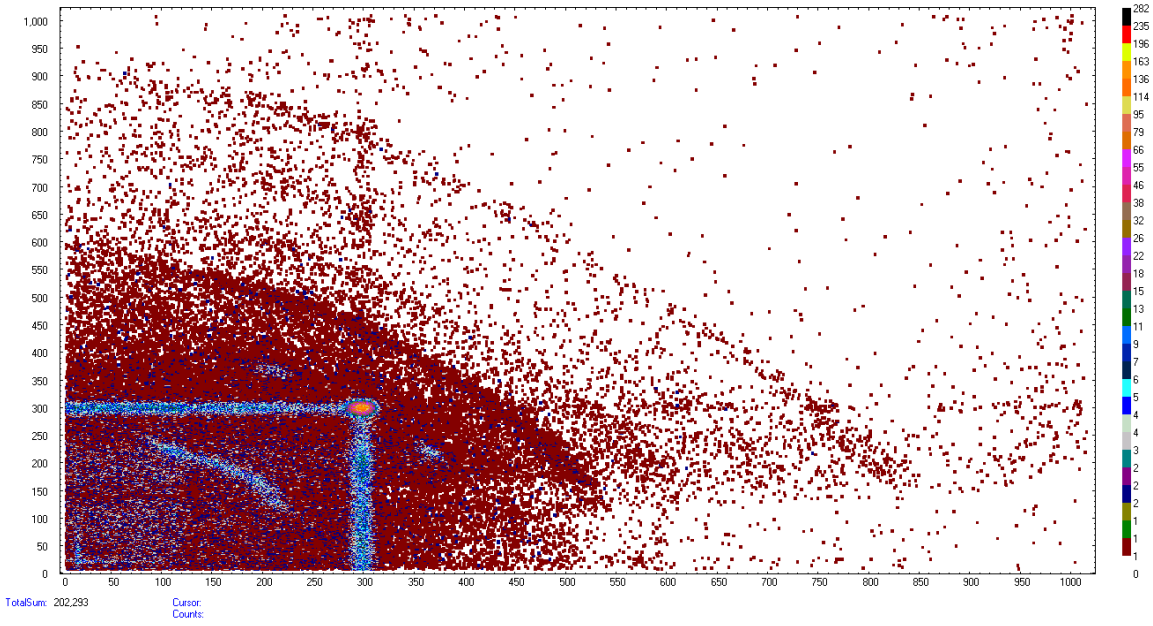

Figure 23: 2D coincidence pulse height spectrum for a neutron energy of 25.915 MeV. The coincidences of 511 keV gamma ray detection can be seen as the orange spot in the lower left. Gamma rays that have Compton scattered before detection are also found in high abundance.

The efficiency of the NaI detectors for detecting 511 keV gamma rays in coincidence for the source geometry used is being determined in a separate experiment. To determine the singles absolute full-peak efficiency of the NaI detector, a thin ^{22}Na source was attached to a silicon detector and placed near the NaI detector, as shown in Figure 24. Positrons emitted from the ^{22}Na source entered the silicon detector where they annihilated. Some of the resultant 511 keV gamma rays were then detected by the NaI detector. The efficiency is the number of events in coincidence between the two detectors divided by the number of positrons detected in the silicon detector.

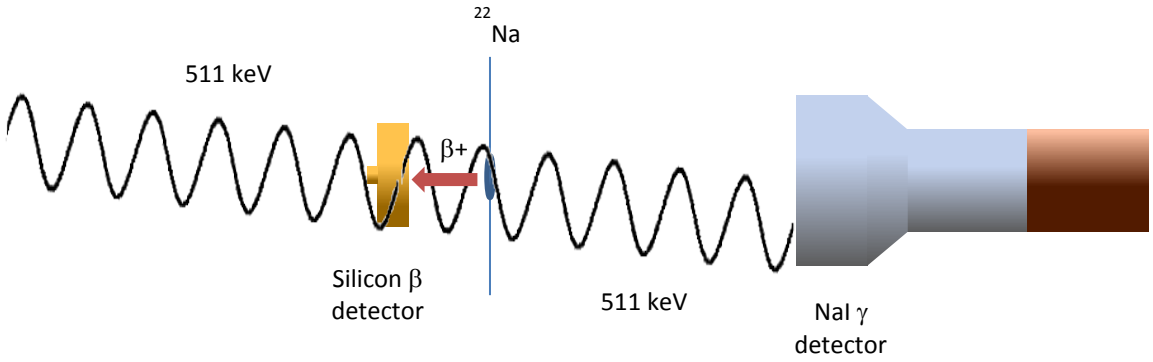

Figure 24: Initial experimental setup for determining the efficiency of the NaI detectors used for ^{11}C decay counting. A ^{22}Na source produces positrons, which annihilate within a silicon detector, producing 511 keV gamma rays. The absolute full-peak detector efficiency is the ratio between the number of coincidences between the two detectors to the number of positrons detected in the silicon detector. Due to additional 1275 keV gamma rays produced by the ^{22}Na source, this result is only valid at large detector distances.

An issue with this measurement is that the ^{22}Na source also emits 1275 keV gamma rays at the same time as positrons. If the 1275 keV gamma ray and the 511 keV gamma ray both enter the detector at the same time, the energy detected would not fall within the cut made around 511 keV. At large detector distances, the probability of this occurring is minimal, but it increases at small distances, which is where the efficiency is needed. To solve this problem, a second NaI detector was placed at a 90° angle to the original detector, as shown in Figure 25, and events were only counted if the 1275 keV gamma ray was detected by this second detector.

Analytical calculations and Monte-Carlo simulations of these experiments were performed to determine the efficiency and compared with the experimental results for a single NaI detector. These

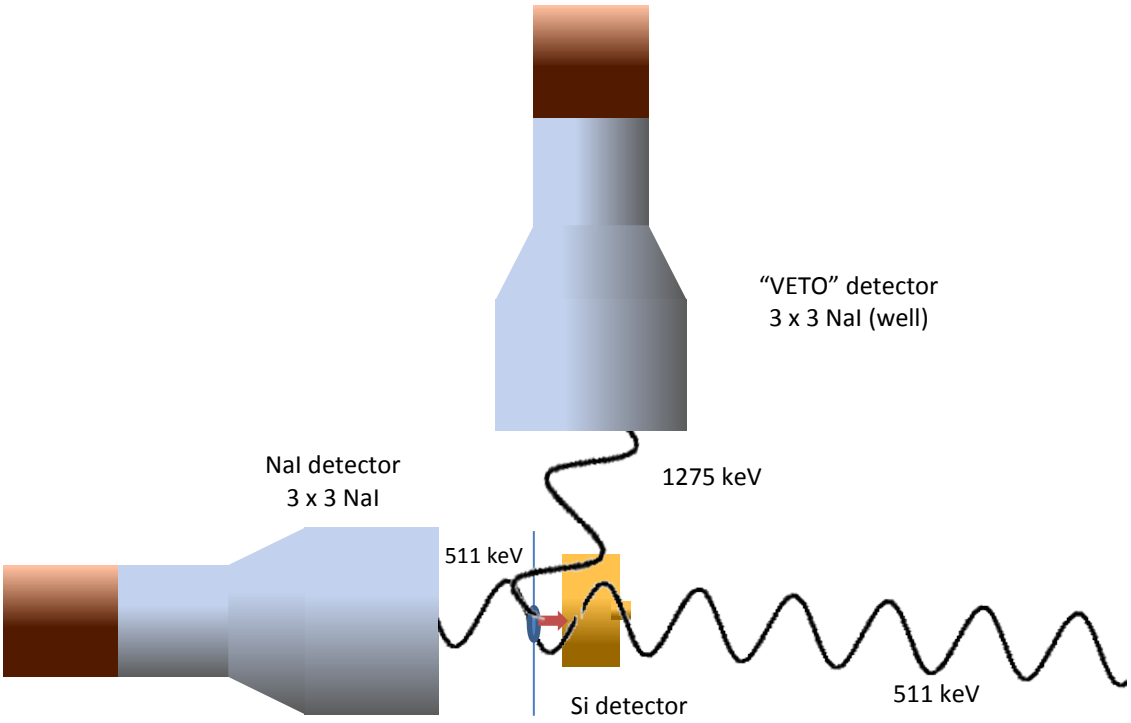

Figure 25: Modified experimental setup to determine the NaI detector efficiency, taking into account the production of a 1275 keV gamma ray concurrently with a positron in the ^{22}Na source. As before, the ^{22}Na source is attached to the silicon detector, with 511 keV gamma rays produced by annihilation within the silicon detector. Only events in which the 1275 keV gamma ray enters the second NaI detector are counted, as it is then known that only the 511 keV gamma could have entered the original NaI detector.

calculations used the technique described in Reference [31]. Once the 1275 keV gamma rays were accounted for, the simulation agreed with measurement, shown in Figure 26. It can be seen that the geometry of the gamma source becomes more important at small distances. At large distances, an extended source looks like a point source. Additionally, the solid angle of the detector is smaller, so it is less likely for the 1275 keV gamma ray to enter the detector. For our activation experiment, with large targets placed flush with the detector face, the geometry needs to be carefully taken into account.

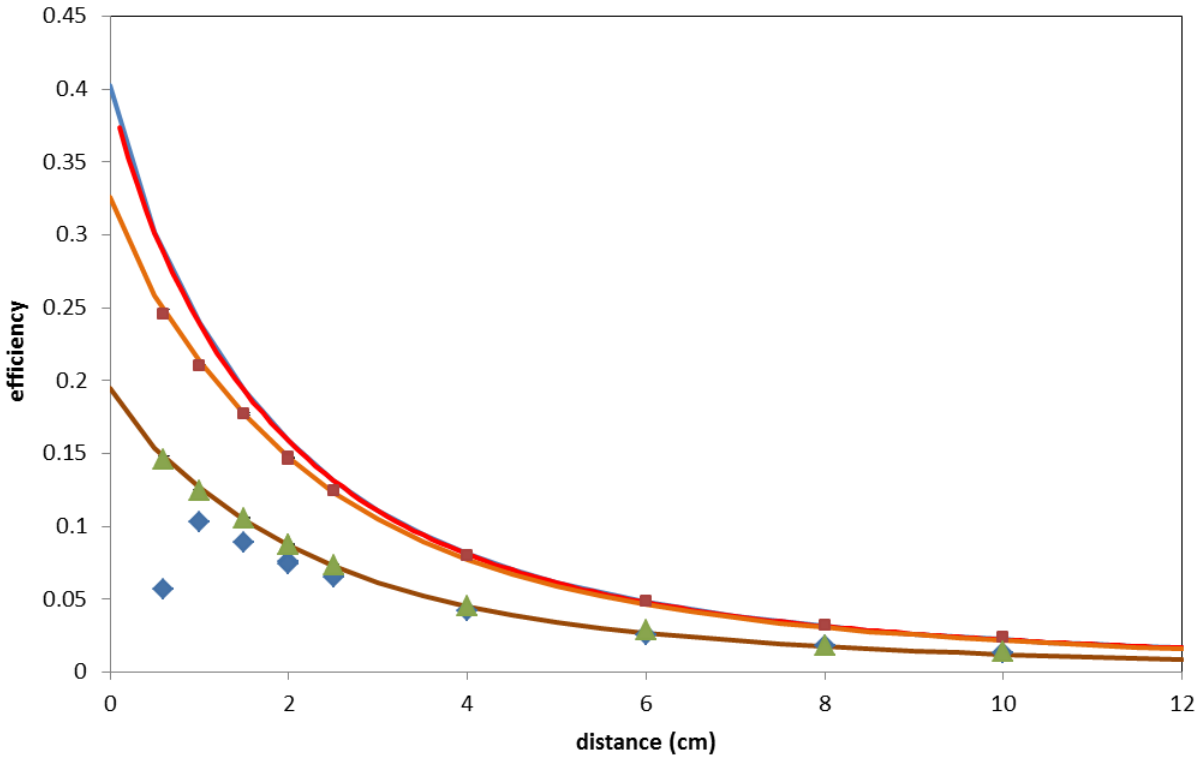

Figure 26: Measured and predicted NaI detector efficiencies. The red and blue lines are the total efficiencies for a point source; the red calculated analytically using Mathcad and the blue using a Monte-Carlo simulation. The orange and green lines are Monte-Carlo simulation of the total and full peak efficiencies, respectively, accounting for an extended source and the detector casing. The blue diamonds are measured full peak efficiencies without correction for the 1275 keV gamma ray, while the red squares and green triangles are, respectively, the total and full peak efficiencies after the 1275 keV gamma ray was accounted for.

This current experiment measures the full-peak efficiency of a single detector; however, the actual efficiency needed is that for two detectors operating in coincidence. To determine the coincidence efficiency, it is planned to add a third NaI detector to the apparatus, as shown in Figure 27, with the silicon detector being replaced with a plastic scintillator to improve the experimental symmetry. This would allow both of the 511 keV annihilation gamma rays, the 1275 keV gamma ray, and the positron annihilation to all be detected concurrently. Monte Carlo simulations of these experiments are being performed and will be validated with experimental results. These simulations will then be extended for source geometries matching that of the polyethylene and graphite targets.

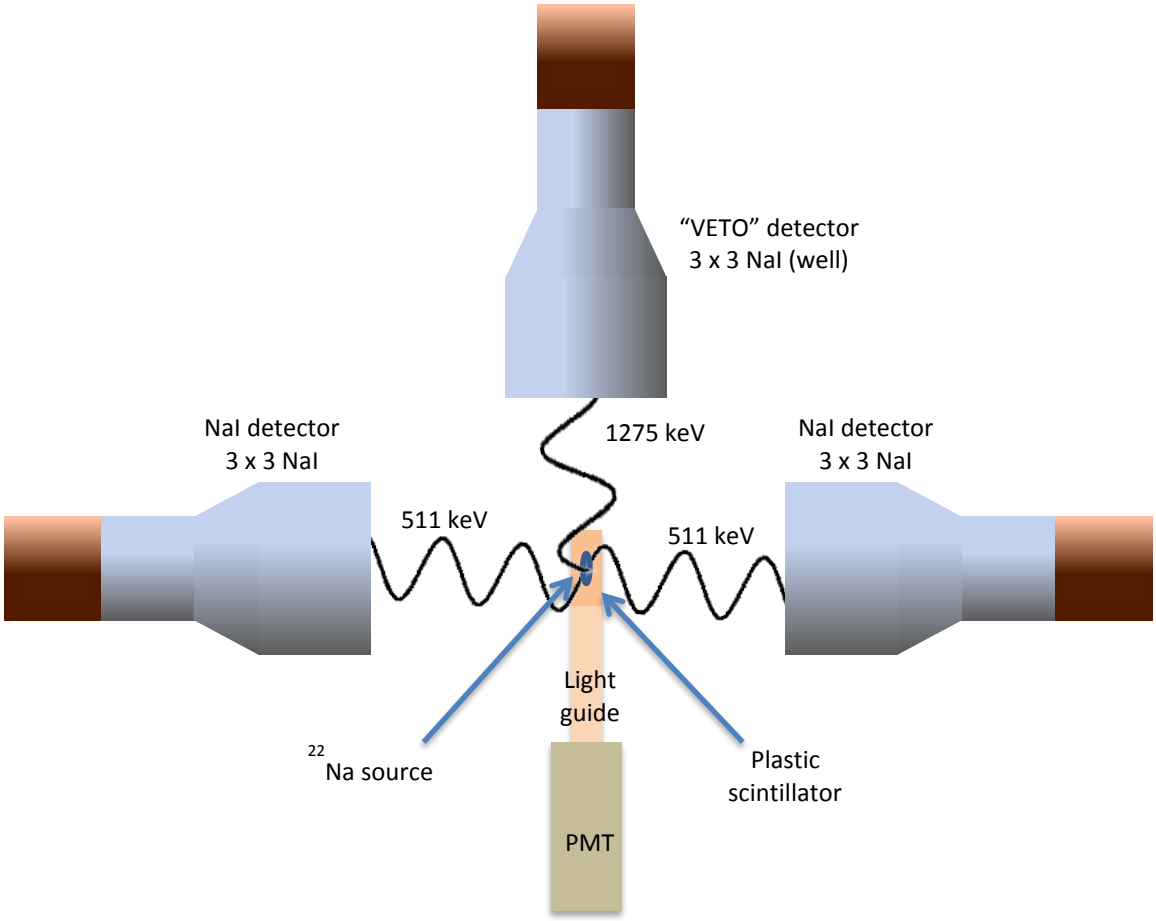

Figure 27: A proposed experiment to measure the coincidence efficiency of the NaI detectors. As in the prior experiments, a ^{22}Na source would produce both a positron, which annihilates within the plastic scintillator detector, and a 1275 keV gamma ray. An additional NaI detector would be added to detect the second 511 keV gamma ray, resulting in a measurement of the coincidence, rather than singles, efficiency.

Chapter 4

DATA ANALYSIS

4.1 Cross-Section

The value of the ^{12}C(n,2n)^{11}C cross-section will be computed using the experimentally determined proton count rates and ^{11}C decay gamma rates. The rate of change of the number of ^{11}C nuclei present during neutron activation is the difference between the rate at which the nuclei are created and the rate at which they decay. Assuming that the neutron flux is constant, this rate of change is given by

$$\frac{dN_{^{11}\mathrm{C}}}{dt} = \langle\sigma_{n,2n}\rangle T_{\mathrm{C}} \frac{N_n}{t} - \lambda N_{^{11}\mathrm{C}}; \tag{18}$$

the first term is the creation rate and the second term is the decay rate. In this equation, $N_{^{11}C}$ is the number of ^{11}C nuclei present, T_C is the thickness of the target in ^{12}C nuclei per unit area, N_n the number of neutrons that hit the target , λ is the decay constant of ^{11}C, and t is the elapsed activation time. Solving for the cross-section gives,

$$\langle\sigma_{n,2n}\rangle = \frac{\lambda N_{^{11}\mathrm{C}}}{T_{\mathrm{C}}(1 - e^{-\lambda t})} \frac{t}{N_n}. \tag{19}$$

During the experiment, the number of protons scattered elastically from the CH_2 target was measured instead of the number of neutrons. This equation can be re-written in terms of N_p, the number of protons detected, as

$$\langle\sigma_{n,2n}\rangle = \frac{\lambda N_{^{11}\mathrm{C}}}{T_{\mathrm{C}}(1 - e^{-\lambda t})} \left(\frac{N_p}{N_n}\right) \frac{t}{N_p}, \tag{20}$$

where the proton to neutron ratio, $\frac{N_p}{N_n}$, is dependent solely upon the geometry of the system and the cross sections of the DT fusion [32] and NP elastic scattering [33] reactions, both of which are well known.

4.2 Proton Count Rate

For each activation run, the number of protons from NP elastic scattering was determined, as shown by the boxed region in Figure 21. The total proton count rate was given by

$$N_p = \frac{N_{p,fg}}{t_{live,fg}} - \frac{N_{p,bg}}{t_{live,bg}}, \tag{21}$$

where $N_{p,fg}$ and $N_{p,bg}$ are the number of detected protons in the foreground and background runs respectively. The live times, $t_{live,fg}$ and $t_{live,bg}$ were given by

$$t_{live} = (\text{total activation time})\left(1 - \frac{\text{coincidences in MPA system}}{\text{coincidences in hardware}}\right). \tag{22}$$

4.3 Number of ^{11}C Nuclei

The total number of ^{11}C nuclei present in the target at the end of activation was determined by fitting either the ^{11}C decay curve, shown in Figure 28, or the ^{11}B growth curve. The decay rates recorded by the MPA system were read into a histogram using the ROOT data analysis libraries [34]. A second histogram containing the growth curve of the total number of decays was also generated. The decay curve was then fit with

$$R(t) = R_0 e^{-\lambda t} + A \tag{23}$$

and the growth curve was fit with

$$N(t) = N_0\left(1 - e^{-\lambda t}\right) + At + B, \tag{24}$$

where R_0 and $R(t)$ are the rate at which the ^{11}C nuclei decays were detected, initially and after time t, respectively, N_0 and $N(t)$ are the total number of decays detected, initially and after time t, respectively, A and B are fit parameters to account for the background count rate, and the decay constant λ was held constant.

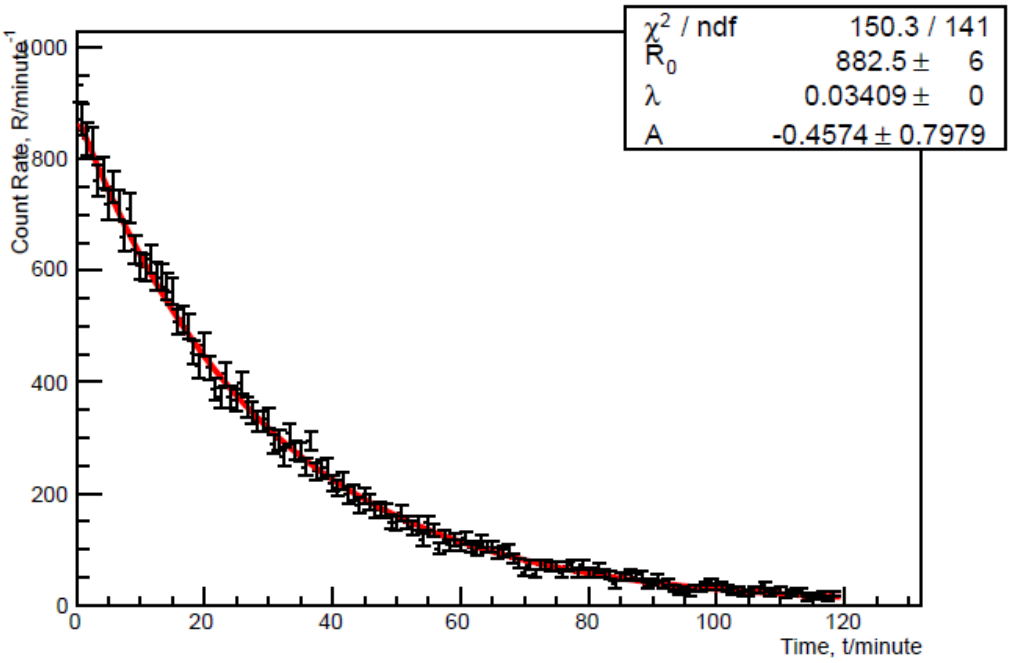

Figure 28: An example of a typical generated ^{11}C decay curve for a neutron energy of 26 MeV. This curve was fit with the function $R(t) = R_0 e^{-\lambda t} + A$ using the ROOT data analysis libraries. The uncertainty in the initial decay rate is typical for larger neutron energies, with larger uncertainties occurring for neutron energies closer to the threshold.

The total number of ^{11}C nuclei that were present in the sample immediately after activation was

$$N_{^{11}\mathrm{C}} = \frac{R_0}{\text{efficiency}} e^{\lambda t_{\text{trans}}} = \frac{N_0}{\lambda \cdot \text{efficiency}} e^{\lambda t_{\text{trans}}}, \tag{25}$$

where t_{trans} is the elapsed time between the end of activation and the beginning of decay counting, and the efficiency is the absolute full peak efficiency of the NaI detectors in coincidence, as determined in Section 3.2.

4.4 Proton to Neutron Ratio

The ratio, $\frac{N_p}{N_n}$ in Equation (20), between the number of neutrons impacting a target and the number of elastically scattered protons detected in the proton telescope can be calculated from the geometry of the system, and the DT fusion [32] and NP elastic scattering [33] cross-sections, both of which are well known. This ratio was analytically calculated using a C++ program.

The energy spectrum and angular distributions of the neutrons hitting the polyethylene and graphite targets and the protons hitting the detector were determined by binning during the evaluation of the integrals

4.4.1 Naïve Method

In the initial method used for determining the neutron to proton ratio, a number of questionable assumptions were made. All of the targets were treated as point sources, and the cross-sections were assumed to be at 0°, as illustrated in Figure 29. Under these conditions, the total number of neutrons impacting the polyethylene target, N_n, given a deuteron energy of E_d and deuteron flux of F_d is

$$N_n(\mathrm{CH_2}) = \sigma_{dt}(0°, E_d) F_d T_t A_t \Omega_{\mathrm{CH_2}} \tag{26}$$

where $\sigma_{dt}(0°, E_d)$ is the cross section of the dt fusion reaction at 0°, T_t is the thickness of the tritium target expressed as the number of ^{3}H nuclei per unit area, A_t is the surface area of the tritium target, and $\Omega_{\mathrm{CH_2}}$ is the solid angle of the polyethylene target relative to the center of the tritium target. The number of neutrons impacting the graphite can be calculated similarly by replacing $\Omega_{\mathrm{CH_2}}$ with $\Omega_{^{12}C}$, the solid angle of the graphite target relative to the center of the tritium target.

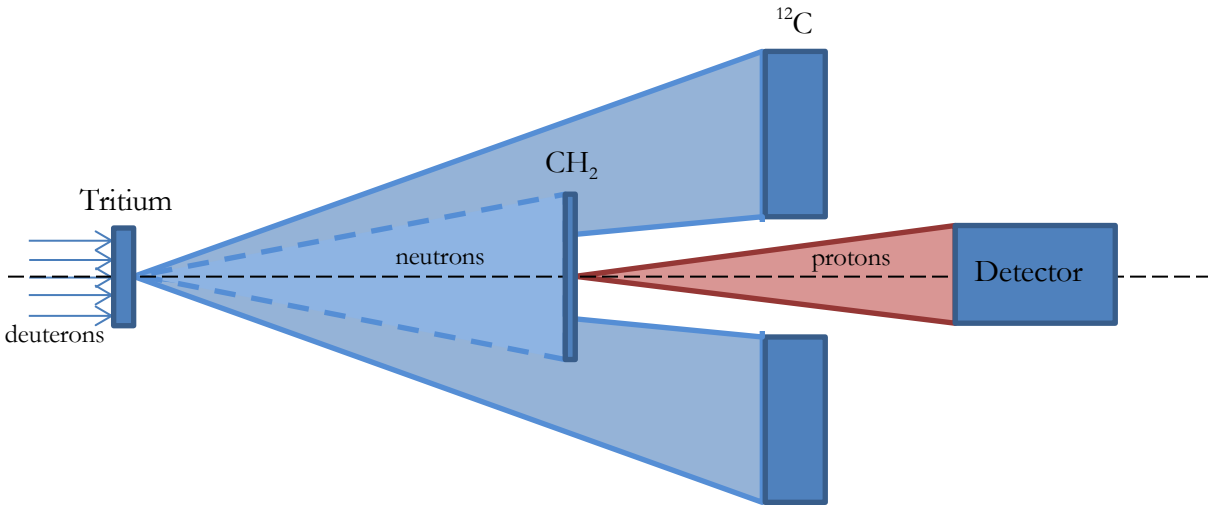

Figure 29: Schematic diagram for the naïve method of calculating the neutron to proton ratio. Neutrons are assumed to be emitted from a single point on the tritium target, as shown by the light blue cones, and protons are likewise assumed to be emitted from a single point on the polyethylene target, shown by the red cone. Additionally, all scattering is assumed to occur at 0°.

Similarly, the total number of protons hitting the detector, N_p, given the neutron energy E_n, is

$$N_p = \sigma_{np}(0°, E_n) N_n(\mathrm{CH_2}) T_{\mathrm{H}}(\mathrm{CH_2}) \Omega_{\mathrm{det}} \tag{27}$$

where $\sigma_{np}(0°, E_n)$ is the np elastic scattering cross section at 0°, $T_{\mathrm{H}}(\mathrm{CH_2})$ is the thickness of the polyethylene target expressed as the number of ^{1}H nuclei per unit area, and Ω_{det} is the solid angle of the proton telescope relative to the center of the polyethylene target.

4.4.2 Extended Targets

A number of corrections were applied to this naïve calculation of the neutron to proton ratio. The first correction accounts for the fact that the targets were not point sources but actually extended targets. The NP elastic scattering and DT fusion cross sections both depend on the scattering angle, shown in Figure 31, and there is also an angular dependence in the energies of the scattered neutrons and protons. To account for these effects, the surface of each target was divided into infinitesimally small

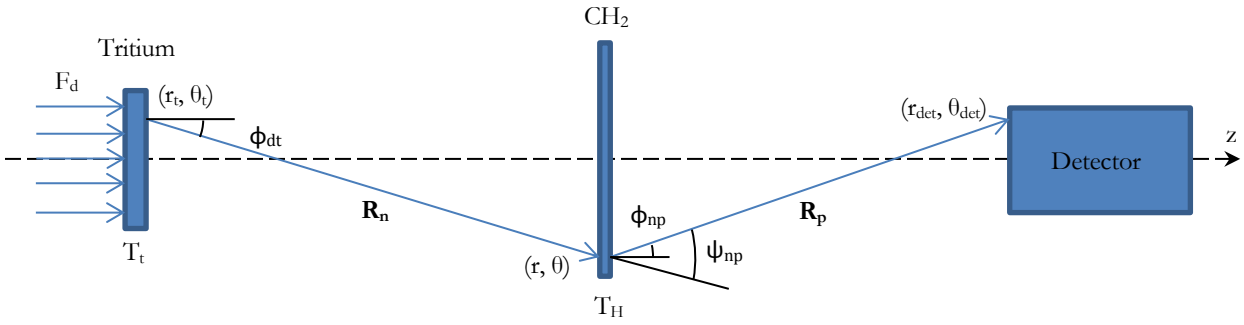

Figure 30: Schematic diagram showing quantities used to calculate the neutron to proton ratio for extended targets. A neutron can travel from an infinitesimal area element at polar coordinates (r_t, θ_t) on the tritium target to an area element at polar coordinates (r, θ) on the polyethylene target along vector $\boldsymbol{R_n}$. A proton can then travel from there to the area element at polar coordinates $(r_{\mathrm{det}}, \theta_{\mathrm{det}})$ on the detector along vector $\boldsymbol{R_p}$. The total number of neutrons or protons can be determined by integrating over the surface of all involved targets. The z coordinate axis is along the center of the beam line.

area elements, each of which were then treated as a point source. The total number of protons or neutrons hitting a target was determined by integrating over the surface area of each target, as depicted in Figure 30. The number of neutrons hitting the polyethylene and graphite targets and protons hitting the detector were binned based upon both scattering angle and energy during the calculation of the integral.

The number of neutrons which hit an area element of the polyethylene target, which come from a specific area element on the tritium target is

$$dN_n(\mathrm{CH_2}) = \sigma_{dt}(\phi_{dt}, E_d) F_d T_t dA_t d\Omega_{\mathrm{CH_2}} \tag{28}$$

where ϕ_{dt} is the DT fusion scattering angle, given by

$$\phi_{dt} = \cos^{-1} \frac{\boldsymbol{R_n} \cdot \hat{\boldsymbol{k}}}{R_n} \tag{29}$$

where $\boldsymbol{R_n}$, the neutron flight path, is the vector from the area element on the tritium target to the area

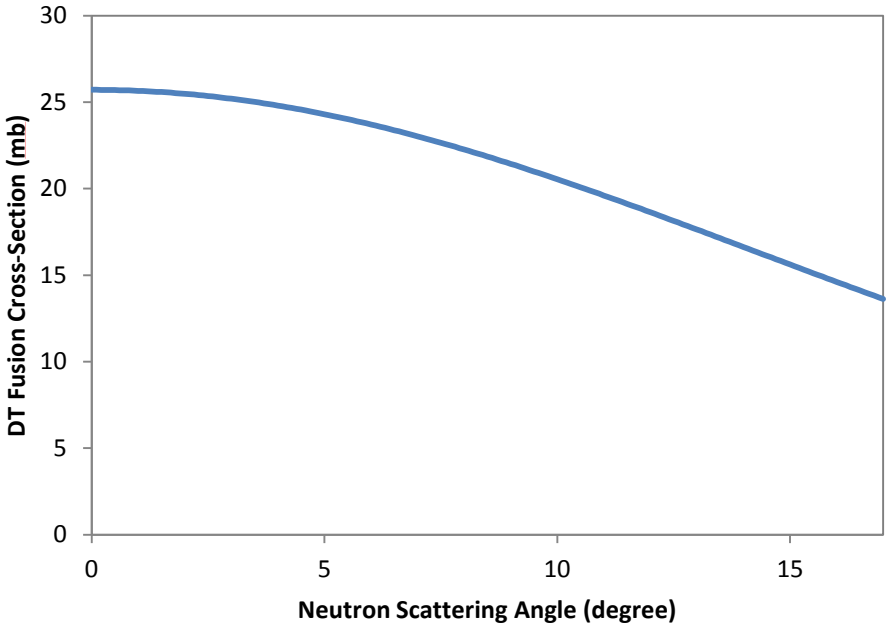

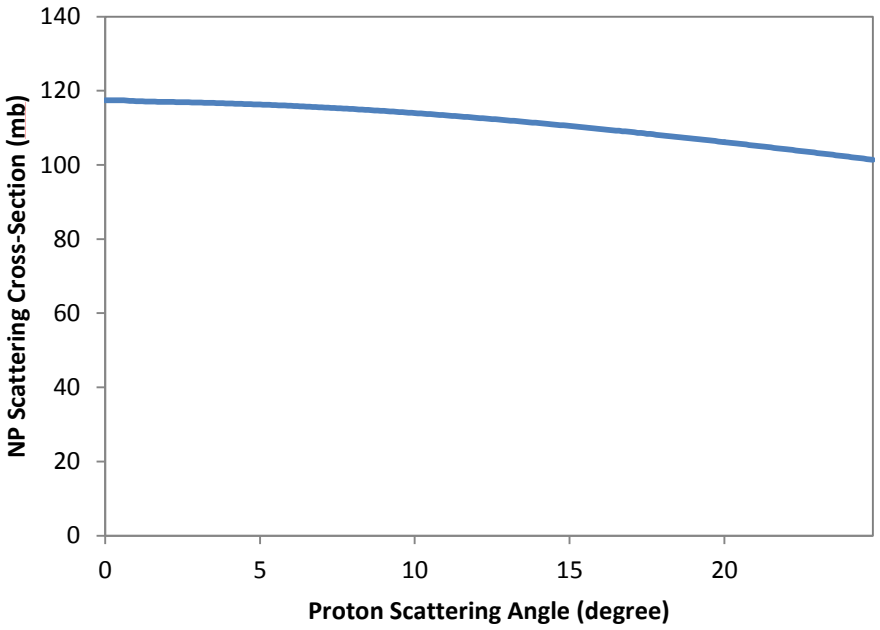

Figure 31: The angular dependence of the DT fusion (top) and NP elastic scattering (bottom) cross-sections. In both cases the cross section is the greatest at an angle of 0° and decreases at larger angles. The DT fusion cross section is for a deuteron energy of 9.07 MeV and the NP scattering cross-section is for a neutron energy of 26.4 MeV. Values were obtained from References 32 and 33.

element on the polyethylene target.

The differential solid angle of a target at a distance $\boldsymbol{r}$ from the target with normal $\hat{\boldsymbol{n}}$ is

$$d\Omega = \frac{\boldsymbol{r} \cdot \hat{\boldsymbol{n}}}{r^3} dA, \tag{30}$$

so the total number of neutrons hitting the polyethylene target is

$$N_n(\mathrm{CH_2}) = \int_0^{2\pi} \int_0^{R} \int_0^{2\pi} \int_0^{R_t} \sigma_{dt}(\phi_{dt}, E_d) F_d T_t \underbrace{r_t dr_t d\theta_t}_{dA_t} \underbrace{\frac{\cos\phi_{dt}}{R_n^{\,2}} r dr d\theta}_{d\Omega_{\mathrm{CH_2}}} \tag{31}$$

where r_t and θ_t are polar coordinates on the tritium target, r and θ are polar coordinates on the polyethylene target, and R_t and R are the radius of the tritium and polyethylene targets, respectively. The number of neutrons impacting the graphite target can be calculated similarly by integrating over the surface area of the graphite target rather than the polyethylene target.

The number of protons that can be detected by an area element of the proton telescope due to elastic scattering from an area element on the CH_2 target is given by

$$dN_p = \sigma_{np}\left(\psi_{np}, E_n(\phi_{dt}, E_d)\right) dN_n(\mathrm{CH_2}) \frac{T_{\mathrm{H}}(\mathrm{CH_2})}{\cos\phi_{dt}} d\Omega_{\mathrm{det}} \tag{32}$$

where $E_n(\phi_{dt}, E_d)$ is the neutron energy, dependent on the deuteron energy and DT scattering angle, and ψ_{np} is the np scattering angle, given by

$$\psi_{np} = \cos^{-1} \frac{\boldsymbol{R_n} \cdot \boldsymbol{R_p}}{R_n R_p} \tag{33}$$

where $\boldsymbol{R_p}$, the proton flight path, is the vector from the area element on the polyethylene target to the area element on the detector.

The total number of protons detected is thus

$$N_p = \int_0^{2\pi} \int_0^{R_{\mathrm{det}}} \int_0^{2\pi} \int_0^{R} \int_0^{2\pi} \int_0^{R_t} \sigma_{np}\left(\psi_{np}, E_n(\phi_{dt}, E_d)\right) \sigma_{dt}(\phi_{dt}, E_d) F_d T_t \frac{T_{\mathrm{H}}(\mathrm{CH_2})}{\cos\phi_{dt}} \underbrace{r_t dr_t d\theta_t}_{dA_t} \underbrace{\frac{\cos\phi_{dt}}{{R_n}^2} r dr d\theta}_{d\Omega_{\mathrm{CH_2}}} \underbrace{\frac{\cos\phi_{np}}{{R_p}^2} r_{\mathrm{det}} dr_{\mathrm{det}} d\theta_{\mathrm{det}}}_{d\Omega_{\mathrm{det}}} \tag{34}$$

where R_{det} is the radius of the detector and ϕ_{np} is given by

$$\phi_{np} = \cos^{-1}\frac{\boldsymbol{R_p}\cdot\hat{\boldsymbol{k}}}{R_p} \tag{35}$$

4.4.3 Graphite Collimation

The hole through the center of the graphite target was slightly too small for all of the protons to pass through unobstructed, thereby causing a collimating effect which must be accounted for. As seen in Figure 32, the distance of a proton from the centerline at a distance z from the polyethylene target is

$$r(z) = \sqrt{x(z)^2 + y(z)^2} \tag{36}$$

where

$$x(z) = \frac{\boldsymbol{R_p}\cdot\hat{\boldsymbol{\imath}}}{\boldsymbol{R_p}\cdot\hat{\boldsymbol{k}}} z + r\cos\theta \tag{37}$$

and

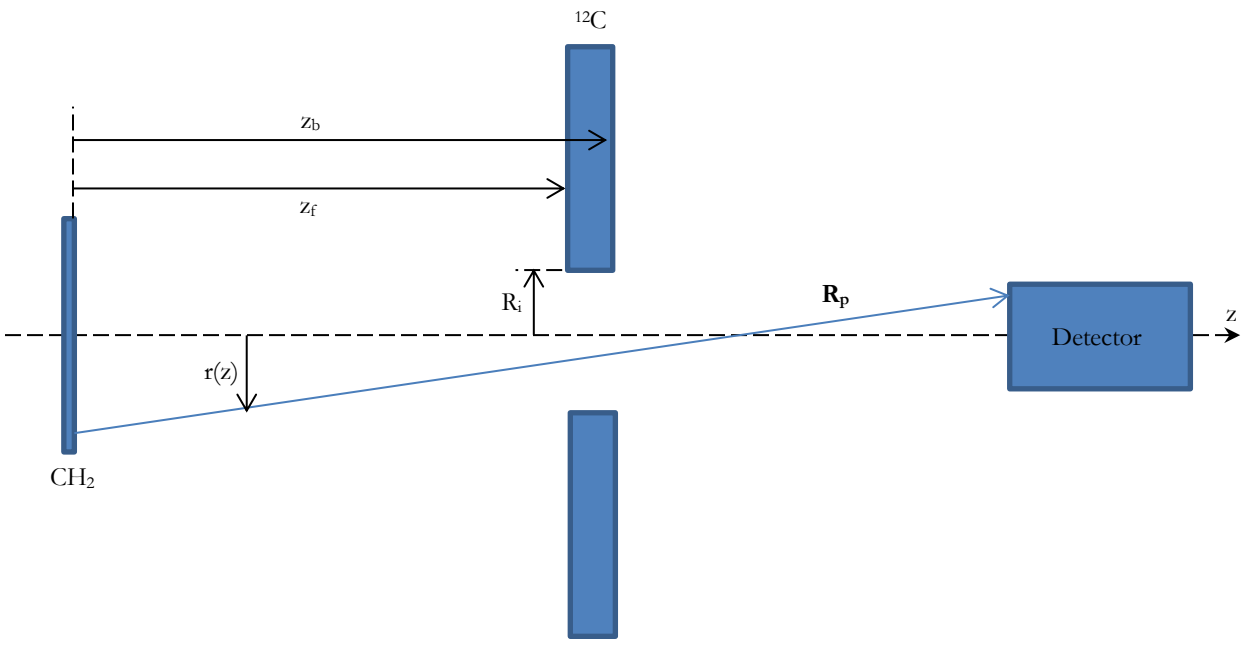

Figure 32: Schematic diagram showing additional quantities used in correction for graphite effects. If the distance $r(z)$ of a proton from the z-axis is greater than R_i, the inner radius of the graphite disk in the range $z_f \le z \le z_b$, then the contribution from that path is excluded from the total integral. The z-axis lies along the center of the beam line.

$$y(z) = \frac{\boldsymbol{R_p} \cdot \hat{\boldsymbol{j}}}{\boldsymbol{R_p} \cdot \hat{\boldsymbol{k}}} z + r \sin\theta. \tag{38}$$

If any path is at a greater distance from the centerline than the inner radius of the graphite, R_i, at the z position of the graphite, it is excluded from the integral. The total number of protons is thus

$$N_p = \int_0^{2\pi} \int_0^{R_{\text{det}}} \int_0^{2\pi} \int_0^{R} \int_0^{2\pi} \int_0^{R_t} \begin{cases} 0, & r(z_f) \ge R_i \text{ or } r(z_b) \ge R_i \\ \sigma_{np}\left(\psi_{np}, E_n(\phi_{dt}, E_d)\right) \sigma_{dt}(\phi_{dt}, E_d) F_d T_t \dfrac{T_{\text{H}}(\text{CH}_2)}{\cos\phi_{dt}} & \end{cases} \\ r_t dr_t d\theta_t \frac{\cos\phi_{dt}}{{R_n}^2} r dr d\theta \frac{\cos\phi_{np}}{{R_p}^2} r_{\text{det}} dr_{\text{det}} d\theta_{\text{det}}, \tag{39}$$

where z_f and z_b are the distances of the front and back of the graphite target, respectively, from the polyethylene target.

A C++ program was written to evaluate these integrals for the numbers of neutrons and protons analytically. Each integral was divided into 150 steps, the number of steps chosen based upon the estimated rate of convergence of the integral as a balance between high accuracy and short run-times. This step size gives around 1% uncertainty in the neutron to proton ratio. The distributions of the scattering energies and angles of protons and neutrons were also calculated by binning on the energy and scattering angle during the evaluation of each integral.

The scattering angles for the DT fusion and NP elastic scattering reactions for each neutron's and proton's path, respectively, were determined during the calculation of the neutron to proton ratio. Figure 33 shows the number of neutrons hitting the polyethylene and graphite targets, from Equation (31), as a function of the DT fusion scattering angle. It can be seen that very nearly all of the neutrons hitting these targets came from reactions with scattering angles other than 0°, as there are many more paths between the two targets with a non-zero scattering angle, with the graphite target having larger angles due to its larger solid angle and hole through the center of the target. No neutron hitting these targets was scattered at an angle of greater than around 17°, corresponding to a drop in the DT fusion cross section of around 13 mb for an incident deuteron energy of 9.07 MeV, as shown in Figure 31.

The number of protons hitting the ΔE detector, from Equation (39), as a function of the NP elastic scattering angle is shown in Figure 34. As with the neutrons, nearly all of the scattering events occurred at angles other than 0°, with no proton being scattered at an angle greater than around 25°, corresponding to a drop in the NP elastic scattering cross section of around 20 mb for an incident proton energy of 26.4 MeV, as shown in Figure 31.

The energy spectra of these protons and neutrons were also determined, as shown in Figure 35 and Figure 36. The neutrons are highly monoenergetic, with variation of less than 0.5 MeV across the surface of the graphite and polyethylene targets, as required for a measurement of the $^{12}C(n,2n)^{11}C$ cross-section as a function of the incident neutron energy. The proton energy spectrum is wider, dropping to zero at around 5 MeV below the peak proton energy. This still allows the protons to be easily identified in the E-ΔE detector.

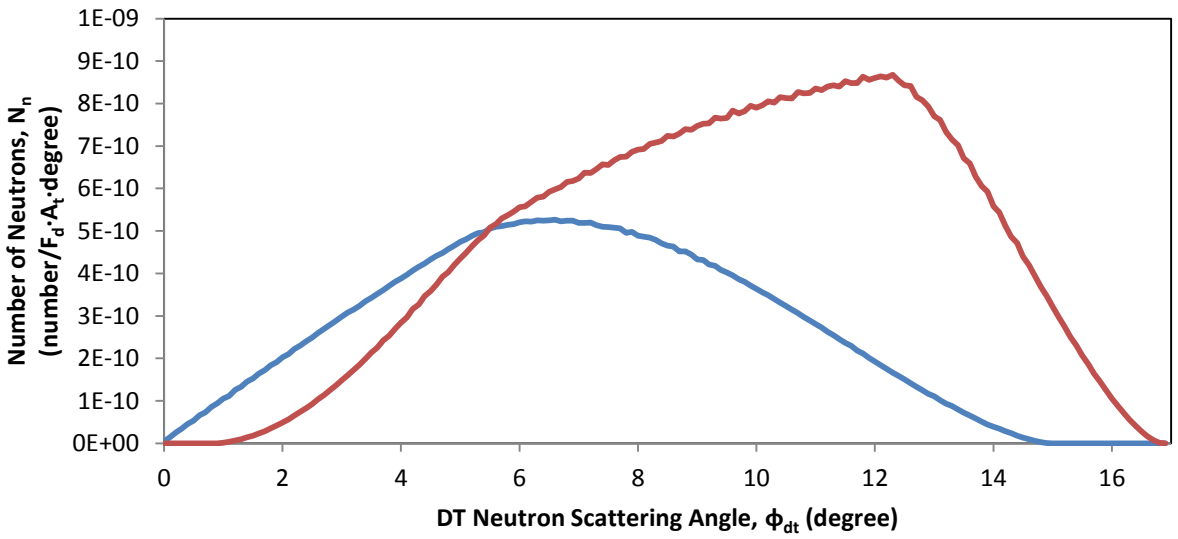

Figure 33: Example of typical predicted number of neutrons hitting the polyethylene and graphite targets as a function of the DT fusion neutron scattering angle for an incident deuteron energy of 9.07 MeV. Neutrons hitting the polyethylene target are shown in blue, and those hitting the graphite in red. It can be seen that most scattering events occur at angles greater than 0°, with higher angles occurring in the graphite than in the polyethylene due to its larger solid angle and hole.

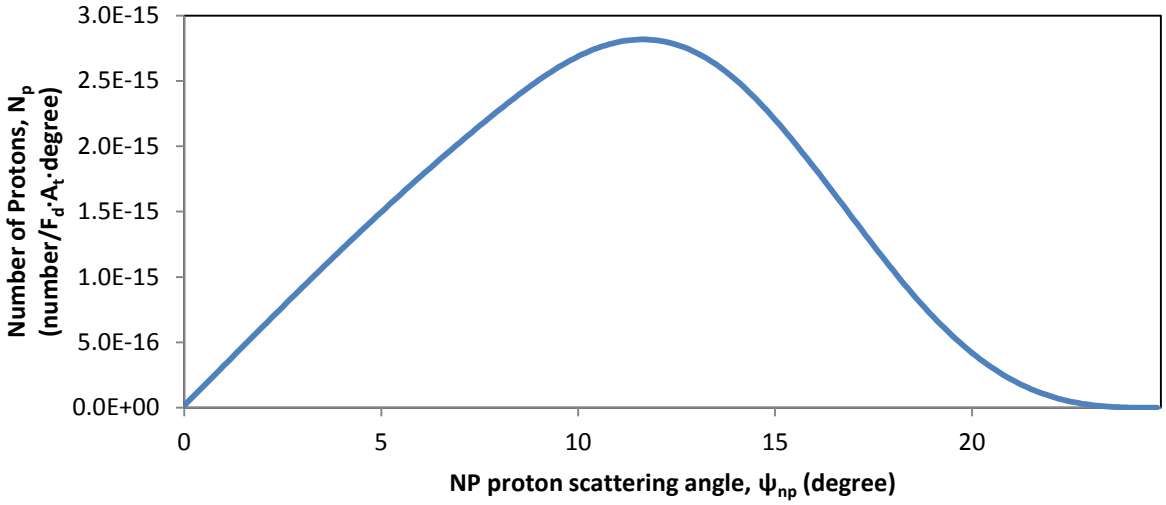

Figure 34: Example of typical predicted number of protons hitting the detector as a function of the np scattering angle for an incident neutron energy of 26.4 MeV. The majority of scattering events occurred at an angle other than 0°, with no proton having been scattered at an angle of greater than 24°.

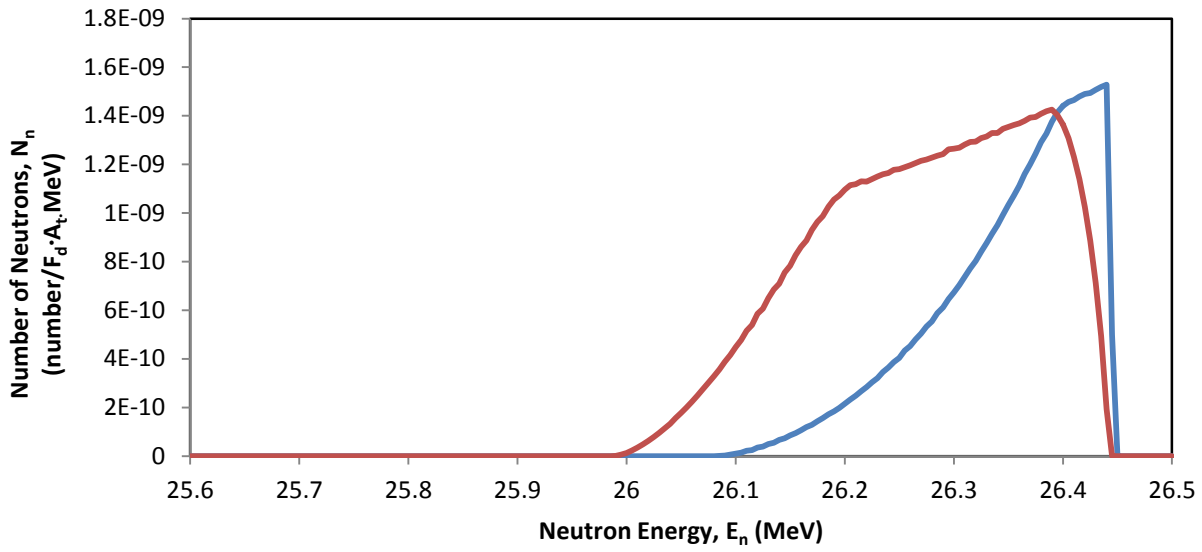

Figure 35: Example of typical predicted number of neutrons hitting the graphite and polyethylene targets as a function of their energy for an incident deuteron energy of 9.07 MeV. Neutrons hitting the graphite target are shown in red, and those hitting the polyethylene in blue. The total variation in neutron energy across the targets is less than 0.5 MeV, one of the design criteria for the experiment.

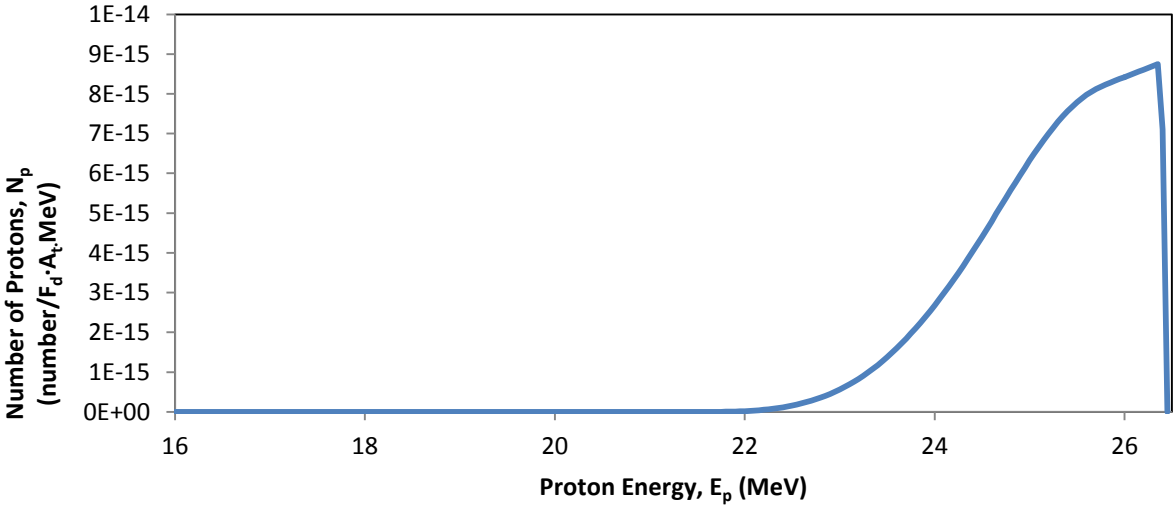

Figure 36: Example of typical number of protons hitting the detector as a function of their energy. The proton rate drops off at energies below the maximum, falling to half of the maximum flux at around 24 MeV for an incident neutron energy of 26.4 MeV.

Chapter 5

RESULTS AND CONCLUSION

5.1 Preliminary Results

Preliminary cross-sections for each run were calculated using Equation (20) using an unvalidated Monte-Carlo simulation to determine the full peak coincidence efficiency of the NaI detectors. The results of this calculation, shown in Figure 37, are much lower than previous measurements, but have the same general shape. Once the experiment described at the end of Section 3.2is implemented, the cross sections will be calculated using the correct values for the coincidence efficiency.

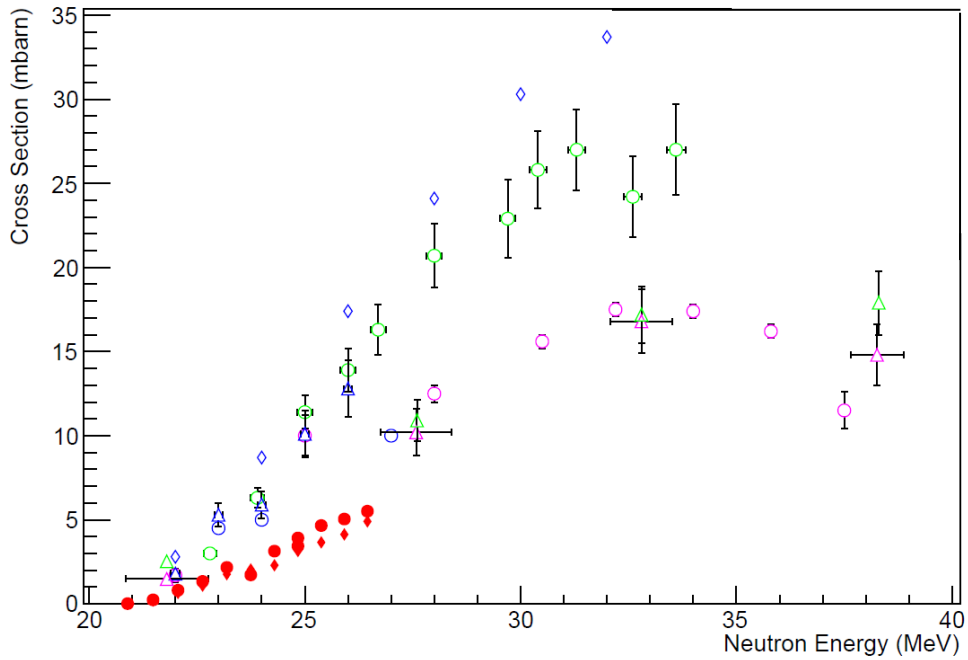

Figure 37: Preliminary cross-sections of the $^{12}C(n,2n)^{11}C$ reaction compared to previous measurements. The empty symbols are previously published data: the blue circles from Brolley et al. [23], the pink circles from Brill et al. [24], the green circles from Anders et al. [25], the blue triangles from Welch et al. [26], the pink triangles from Soewarsono et al. [27], the green triangles from Uno et al. [28], and the blue diamonds from Dimbylow [29]. The solid red symbols are our preliminary results: the circles are from the polyethylene target and the diamonds from the graphite target.

5.2 Conclusion

In this experiment, a measurement of the cross-section of the $^{12}C(n,2n)^{11}C$ cross-section was performed for the energy range of 20-26 MeV. Four different techniques for determining this cross section were considered, as described in Section 2.2; the measurement of prompt de-activation gamma rays, the detection of both of the produced neutrons, the detection of recoil ^{11}C nuclei, and the same activation technique used in other measurements. Each of these has advantages and disadvantages, but only the activation technique was deemed feasible.

Neutrons were produced via the T(d,n)α reaction by bombarding a titanium tritide target with deuterons using the tandem van der Graaff accelerator at Ohio University. These neutrons were allowed to strike both polyethylene and graphite targets, with the neutron flux being determined indirectly via NP elastic scattering from the polyethylene target. After activation, the ^{11}C decay rate was measured using back-to-back NaI detectors in coincidence. The cross-section was then determined from the number of ^{11}C nuclei created, the number of protons detected, and the ratio between the number of neutrons hitting a target and the number of protons detected.

The ratio between the number of neutrons and protons was determined based on the geometry of the system and the cross sections of the DT fusion and NP elastic scattering reactions. The surface of each of the targets was divided into infinitesimal area elements and integrated over every possible neutron and proton path through the system. The effects of varying cross-sections and the collimation of the protons by the graphite target were accounted for.

To determine the number of ^{11}C nuclei present in the target from the number of decays detected, the absolute full peak coincidence efficiency of the NaI detectors is being determined. A separate experiment was performed to determine the singles efficiency of the detector, and it is planned to extend this to measure the coincidence efficiency. The measurement of this efficiency is currently the only thing preventing the final determination of the $^{12}C(n,2n)^{11}C$ cross-section.

It is hoped that the $^{12}C(n,2n)^{11}C$ cross-section will be used as part of a diagnostic tool for inertial confinement fusion. By placing one or more pieces of graphite in the reaction chamber and afterwards measuring the ^{11}C activation, the number of tertiary neutrons (those with energies higher than 14.1 MeV) can be determined.

Appendix A

CODE LISTING

A C++ program was written to calculate the cross-sections as described in Chapter 4 using the ROOT data analysis libraries developed by CERN [34].

A.1 recalculate_all.C

The function defined in this file calculates the cross-section for every pair of runs listed in '`C:\root\macros\n2n\2013 Ohio Run Data\ROOT Data\Cross Sections 2013.csv`' from the recorded MPA data.

```
void recalculate_all()
{
    char const * root_data = "C:\\root\\macros\\n2n\\2013 Ohio Run
Data\\ROOT Data";
    char const * cross_sections = gSystem->PrependPathName( root_data,
"Cross Sections 2013.csv" );
    char const * run_summary = gSystem->PrependPathName( root_data,
"Run Summary 2013.csv" );
    char const * control_room = gSystem->PrependPathName( root_data,
"Control Room Protons" );
    char const * counting_station = gSystem->PrependPathName(
root_data, "Counting Station" );

    gROOT->LoadMacro( "n2n/CrossSection_loadsum.cxx" );
    gROOT->LoadMacro( "n2n/CrossSection_calculate.cxx" );
    gROOT->LoadMacro( "n2n/RunSummary.cxx" );
    gROOT->LoadMacro( "n2n/CSVFile.cxx" );
    gROOT->LoadMacro( "n2n/Uncertain.cxx" );
    gROOT->LoadMacro( "n2n/proton.cxx" );
    gROOT->LoadMacro( "n2n/decay.cxx" );

    if ( gSystem->AccessPathName( cross_sections ) )
    {
        cerr << "Cannot access file: " << cross_sections << endl;
        return;
    }


    if ( gSystem->AccessPathName( run_summary ) )
    {
```

```
            cerr << "Cannot access file: " << run_summary << endl;
            return;
        }

        n2n::CrossSection * cross = new n2n::CrossSection();
        cross->Load( cross_sections );

        n2n::RunSummary * sum = new n2n::RunSummary();
        sum->Load( run_summary );
        for ( int i = 3; i < cross->NumRows(); ++i )
        {
            vector<string> row = cross->GetRow( i );
            int fg_run = atoi( row[n2n::CS_FG_RUN_NUMBER].c_str() );
            int bg_run = atoi( row[n2n::CS_BG_RUN_NUMBER].c_str() );
            sum->UpdateRunProtons( control_room, fg_run );
            sum->UpdateRunProtons( control_room, bg_run );
            sum->UpdateRunC11( counting_station, fg_run );
        }
        cross->LoadSummary( sum );
        sum->Save( run_summary );
        delete sum;

        cross->Calculate();
        cross->Save( cross_sections );
        delete cross;
    }
```

A.2 plot_cross_sections.C

The function defined in this file, `void plot_cross_sections()`, creates a plot of the calculated cross-sections, optionally including the previously measured values. There are three macros, `GROWTH_CURVE`, `DECAY_CURVE`, and `PRIOR_DATA`, which control the sources of data included in the final graph. The previously published data is hardcoded into the file and our calculations are read from the file '`C:\root\macros\n2n\2013 Ohio Run Data\ROOT Data\Cross Sections 2013.csv`'.

A.3 CrossSection.hxx

This file declares a class, `struct CrossSection`, which provides abstract access to the '`Cross Sections 2013.csv`' file. The method '`LoadSummary`' copies relevant values from the '`Run Summary 2013.csv`' file and the method '`Calculate`' calculates the cross sections.

```
#include "CSVFile.hxx"
```

```
#include "RunSummary.hxx"
#include "Uncertain.hxx"

namespace n2n {

/* This is a horrible way to define constants, but ROOT will crash if
 * they are defined in a more reasonable way. */
namespace geometry {

// cross-sectional area (cm^2)
const UncertainD area_disk()     { return UncertainD( 43.257 ); }
const UncertainD area_shield()   { return UncertainD( 43.257 ); }
const UncertainD area_plastic()  { return UncertainD( 5.067 ); }
const UncertainD area_detector() { return UncertainD( 1.5 ); }

// thickness (cm)
const UncertainD thickness_disk()     { return UncertainD( 0.89 ); }
const UncertainD thickness_shield()   { return UncertainD( 0.38 ); }
const UncertainD thickness_plastic()  { return UncertainD( 0.164 ); }

// distance (cm)
const UncertainD distance_de() { return UncertainD( 0.481 ); }

} // namespace geometry

#define DIST_DE  0.481  ///< Distance of dE detector behind front of
detector assembly (cm)

/** Cross Section file column names */
enum CSFields { ... };

struct CrossSection : public CSVFile
{
    public:
        /** Copy values from Run_Summary.csv file into the
         * Cross_Sections.csv file
         * @param summary The run summary file to use */
        void LoadSummary( RunSummary const * const summary );

        /** Calculate cross sections based on the values in
         * Cross_Sections.csv */
        void Calculate();
};

} // namespace n2n
```

A.4 RunSummary.hxx

This file declares a class, `struct RunSummary`, which provides abstract access to the '`Run Summary 2013.csv`' file. The methods '`UpdateRunProtons`' and '`UpdateRunC11`' update, respectively, the number of protons or ^{11}C nuclei for a given run number using the MPA data stored in the given directory.

```
#include "CSVFile.hxx"

namespace n2n {

#define EFFICIENCY_SHIELD  ...
#define EFFICIENCY_DISK    ...
#define EFFICIENCY_PLASTIC ...

/** Run summary column names */
enum RSFields { ... };

struct RunSummary : public CSVFile
{
    public:
        /** Retrieve a run by number.
         * @param run_number The run to retrieve.
         * @return The requested run. */
        vector<string> GetRun( int run_number ) const;

        /** Save a run by number.
         * @param run_number The run to save.
         * @param row The values to write. */
        void SetRun( int run_number, vector<string> const & row );

        /** Get the number of runs in the file */
        int NumRuns() const;

        /** Update the number of protons for a run.
         * @param dirname The directory containing the MPA data.
         * @param run_number The run to save. */
        void UpdateRunProtons( char const * dirname, int run_number );

        /** Update the number of 11C nuclei for a run.
         * @param dirname The directory containing the MPA data.
         * @param run_number The run to save. */
        void UpdateRunC11( char const * dirname, int run_number );
};

} // namespace n2n
```

A.5 CSVFile.hxx

This class, `struct CSVFile`, which is the base class of both `struct CrossSection` and `struct RunSummary`. It provides methods for both reading from and writing to a CSV formatted file.

```
#include <vector>

namespace n2n {

/** @brief Easy access to CSV formatted data. */
struct CSVFile
{
    public:
       /** Load a file containing csv foramtted data.
        * @param filename The file to load. */
       void Load( char const * filename );

       /** Save a file containing csv formatted data.
        * @param filename The file to save to. */
       void Save( char const * filename ) const;

       /** Retrieve a row from the file.
        * @param row_number The row to retrieve.
        * @return The requested row. */
       vector<string> GetRow( int row_number ) const;

       /** Overwrite a row in the file.
        * @param row_number The row to overwrite.
        * @param row The values to write. */
       void SetRow( int row_number, vector<string> const & row );

       /** Get the number of rows in the file. */
       int NumRows() const;

    private:
       vector<string> data_;

       /** Parse a string containing a csv formatted row.
        * @param row_str The string to parse.
        * @return A vector of values in the string.  */
       static vector<string> ParseRow( string row_str );

       /** Format values into a csv formatted row.
        * @param row_vec The values to format.
        * @return A string containing those values. */
       static string FormatRow( vector<string> row_vec );
};

} // namespace n2n
```

A.6 proton.hxx

This file declares the methods used to calculate the number of protons from NP elastic scattering. The functions '`ParseDataFile`' and '`ParseHeaderFile`' read, respectively, the .csv and .mpa files containing data from the protons telescope and '`CountsInRegion`' calculates the number of protons.

```
#include "Region.hxx"

namespace n2n {

/** @brief Functions to calculate proton counts. */
namespace proton {

/** Parse the .csv data file produced by MPA4 for the proton telescope.
 * @param filename The path to the file.
 * @return A 2D-histogram containing the data as a dE-E plot. */
TH2I * ParseDataFile( char const * const filename );

/** Parse the .mpa file produced by MPA4 for the proton telescope.
 * @param filename The path to the file.
 * @return The region of interest for the run. */
Region ParseHeaderFile( char const * const filename );

/** Determine the total number of counts in the region of interest.
 * @param data The dE-E data.
 * @param roi The region of interest.
 * @return The number of counts in the region. */
Int_t CountsInRegion( TH2I const * const data, Region const & roi );

} // namespace proton
} // namespace n2n
```

A.7 decay.hxx

This file declares functions used to calculate the number of ^{11}C nuclei present in a target after activation. It provides methods to perform this calculation both with decay curves, using Equation (23), and growth curves, using Equation (24). In each of the two namespaces, the function '`ParseDataFile`' reads the MPA data file, '`FitDecayCurve`' performs a fit with the appropriate function, and '`Counts`' returns the calculated number of ^{11}C nuclei.

```
#include "Uncertain.hxx"

namespace n2n {
```

```
/** @brief Functions used to calculate ^11C decays. */
namespace c11 {

/** @brief Calculation using decay curves. */
namespace decay {

/** Parse a decay curve given in a tab-separated file into a TGraphErrors
 * object.
 *
 * @param filename The file to read. This input file should be the output of
 *   the MPA4 software set to its CSV output mode and contain data from a
 *   decay curve.
 * @param deadtime A file containing the deadtime corrections in CSV format.
 * @param dt_col1 The column in deadtime that contains corrections for the
 *   first NaI detector.
 * @param dt_col2 The column in deadtime that contains corrections for the
 *   second NaI detector.
 *
 * @return A TGraphErrors object containing the input decay curve.
 * The error is calculated to be the square root of the number of counts. */
TGraphErrors * ParseDataFile( char const * filename, CSVFile * deadtime,
                              int dt_col1, int dt_col2 );

/** Fit an exponential decay curve to a TGraphErrors object.
 * The decay curve is given by N_0 e^{-λt} + A.
 *
 * @param ge The TGraphErrors object to be fit.
 * @return A TFitResultPtr containing the results of the fit. */
TFitResultPtr FitDecayCurve( TGraphErrors * ge );

/** Calculate the total number of C11 originally in the sample, N_C11.
 *       N_C11 = N_0 e^{λ t_trans} / λ
 *       δ_{N_C11} = δ_{N_0} e^{λ t_trans} / λ
 *
 * @param fr The TFitResultPtr returned by FitDecayCurve.
 * @param trans_time The elapsed time before counting began, t_trans.
 * @return The total number of C11 originally present in the sample. */
UncertainD Counts( TFitResultPtr fr, double trans_time );

} // namespace decay


/** @brief Calculatuion using growth curves */
namespace growth {

/** Parse a decay curve from a tab-separated file into a TGraphErrors growth
 *   curve.
 *
 * @param filename The file to read. This should be the CSV output of the
```

```
 *   MPA4 software.
 * @param deadtime A file containing the deadtime corrections in CSV format.
 * @param dt_col1 The column in deadtime that contains corrections for the
 *   first NaI detector.
 * @param dt_col2 The column in deadtime that contains corrections for the
 *   second NaI detector.
 *
 * @return The growth curve. Uncertainty is the square root of counts. */
TGraphErrors * ParseDataFile( char const * filename, CSVFile * deadtime,
                              int dt_col1, int dt_col2 );

/** Fit an exponential growth curve to the TGraphErrors object.
 * The growth curve is given by R_0(1 - e^{λt}) + At + B.
 *
 * @param ge The TGraphErrors object ro fit.
 * @return A TFitResultPtr containing the results of the fit. */
TFitResultPtr FitGrowthCurve( TGraphErrors * ge );

/**
 * Calculate the total number of ^11C originally in the sample, N_C11.
 *       N_C11 = R_0 e^{λ t_trans}
 *       δ_{N_C11} = δ_{R_0} e^{λ t_trans}
 *
 * @param fr The TFitResultPtr returned by FitGrowthCurve.
 * @param trans_time The elapsed time before counting began, t_trans.
 * @return The total number of ^11C originally in the sample. */
UncertainD Counts( TFitResultPtr fr, double trans_time );

} // namespace growth

} // namespace c11
} // namespace n2n
```

References

[1] A. Einstein, Ann. d. Phys. **17**, 891 (1905).

[2] F. W. Aston, Nobel Lecture, December 12, 1922.

[3] A. S. Eddington, *Stars and Atoms*. (Oxford University Press, London, 1928), pp. 99-106.

[4] F. W. Aston, Proc. R. Soc. Lond. A **163**, 391 (1937).

[5] K. T. Bainbridge and E. B. Jordan, Phys. Rev. **50**, 282 (1936).

[6] J. Mattauch, Phys. Rev. **50**, 617 (1936).

[7] M. S. Livingston and H. A. Bethe, Rev. Mod. Phys. **9**, 245 (1937).

[8] J. D. Lawson, Proc. Phys. Soc. B **70**, 6 (1957).

[9] W. H. Bennett, Phys. Rev. **45**, 890 (1934).

[10] R. F. Post, Proc. 2nd UN Intl. Conf. Peaceful Atm. Energ. **32**, 245 (1958).

[11] R. Gunn, Phys. Rev. **33**, 832 (1929).

[12] L. Spitzer Jr., Proc. 2nd UN Intl. Conf. Peaceful Atm. Energ. **32**, 181 (1958).

[13] M. N. Rosenbluth, Proc. 2nd UN Intl. Conf. Peaceful Atm. Energ. **31**, 85 (1958).

[14] E. P. Butt et al., Proc. 2nd UN Intl. Conf. Peaceful Atm. Energ. **32**, 42 (1958).

[15] G.G. Dolgov-Saveljev et al. Sov. Phys. JETP **11**, 287 (1960)

[16] http://www.efda.org/JET/; http://www.ccfe.ac.uk/JET.aspx

[17] http://www.iter.org

[18] E. Teller and S. Ulam, Los Alamos Report LAMS-1225, 1951 (unpublished).

[19] W. D. Metz, Science **117**, 1180 (1972).

[20] LLE Review **69**, 46 (1996).

[21] S. Skupsky and S. Kacenjar, J. Appl. Phys. **52**, 2608 (1961).

[22] D. R. Welch, H. Kislev, and G. H. Miley, Rev. Sci. Instrum. **59**, 610 (1988).

[23] J. E. Brolley Jr., J. L. Fowler, and L. K. Schlacks, Phys. Rev. **88**, 618 (1952).

[24] O. D. Brill, N. A. Vlasov, S. P. Kalnin, and L. S. Sokolov, Sov. Phys. Doklady **6**, 24 (1961).

[25] B. Anders, P. Herges, and W. Scobel, Z. Phys. A **301**, 353 (1981).

[26] P. Welch, J. Johnson, G. Randers-Pehrson, and J. Rapaport, Data file EXFOR-12912.004, compare Bull. Am. Phys. Soc. **26**, 708 (1981).

[27] T. S. Soewarsono, Y. Uwamino, and T. Nakamura, JAERI Tokai Rep. **27**, 354 (1992).

[28] Y. Uno, Y. Uwamino, T. S. Soewarsono, and T. Nakamura, Nucl. Sci. Eng. **122**, 27 (1996).

[29] P. J. Dimbylow, Phys. Med. Biol. **25**, 637 (1980).

[30] H. Vonach, A. Pavlik, M. B. Chadwick, R. C. Haight, R. O. Nelson, S. A. Wender, and P. G. Young, Phys. Rev. C **50**, 1953 (1994).

[31] S. Yalcin, O. Gurler, G. Kaynak, and O. Gundogdu, Appl. Rad. and Isotopes **65**, 1179 (2007).

[32] M. Drosg, IAEA report IAEA-NDS-87 Rev. 5 (2000).

[33] V. G. J. Stoks, R. A. M. Klomp, M. C. M. Rentmeester, and J. J. de Swart, Phys. Rev. C 48, 792 (1993); Computer code NN-OnLine <http://www.nn-online.org>.

[34] R. Brun and F. Rademakers, presented at AIHENP, Lausanne, Switzerland, 1996 (unpublished).